Olfactory combinatorial coding supports risk-reward decision making in *C. elegans*

Md Zubayer Hossain Saad[1], William G. Ryan V[2], C. Autumn Edwards[1], Benjamin N. Szymanski[1], Aryan R. Marri[1], Lilian G. Jerow[1, 3], Robert McCullumsmith[2], and Bruce A. Bamber[1,4]

1. Department of Biological Sciences, The University of Toledo
2. Department of Neurosciences, The University of Toledo
3. Current address: Neuroscience Graduate Program, University of Cincinnati
4. Corresponding Author

Acknowledgements: We would like to thank Shawn Lockery and Dirk Albrecht for invaluable help and materials for the microfluidics behavioral assays, the *C. elegans* Genetics Center for strains, Tomer Avidor-Reiss and Qian Chen for assistance with confocal microscopy, and the University of Toledo Office of Research for funding support through the DeArce-Koch Memorial Foundation Award and the Interdisciplinary Research Initiation Award

Abstract
Vertebrate and insect olfactory systems generate diversity in odor perception using combinatorial coding, where individual odorant molecules activate unique but overlapping sets of olfactory receptor neurons. It is not well understood how these patterns are decoded and transformed into downstream physiological responses. Here, we demonstrate that *Caenorhabditis elegans* uses combinatorial coding to formulate locomotory responses to the odorant 1-octanol (1-oct). Whole-network Ca^{++} imaging showed that 1-oct is encoded combinatorially, activating multiple sensory neurons including ASH and AWC, associated with repulsion and attraction, respectively. The temporal dynamics of these neuronal activations indicate that 1-oct stimulates attractive and repulsive afferent pathways simultaneously; altering the relative strengths of these pathways is sufficient to convert 1-oct from a repellent to an attractant in microfluidics-based behavioral assays. These results identify the balance between attraction and repulsion as a key factor determining chemotactic behavior, achieved through modulation of locomotory reversals and speed. At the circuit level, the attractive and repulsive pathways can both entrain the activity of the reverse command interneuron AVA, a key regulator of reversals, with the stronger pathway predominating. This coding strategy facilitates context-dependent modulation of sensory responses. 1-oct is present in decaying plant material, signaling the possible presence of bacterial food. However, 1-oct is also toxic, and therefore represents a high risk food signal. Adding a different food signal (representing better food in a different location) suppresses the 1-oct attraction pathway by depressing AWC activity, tips the sensory balance toward the aversive pathway, and converts 1-oct attraction into 1-oct repulsion.

Running title: The balance of attraction and repulsion in chemotaxis

Introduction

Animals must detect and discriminate chemical signals in the environment and stimulate downstream perceptual and physiological responses to find food, avoid hazards, and find mates. A relatively simple strategy is labeled line coding, in which a specific sensory stimulus activates a class of dedicated receptor neurons that are hard-wired to produce a specific perception or response, as typified by the vertebrate gustatory system (Mueller et al., 2005, Yarmolinsky et al., 2009, Barretto et al., 2015, Roper and Chaudhari, 2017). A more sophisticated strategy is combinatorial coding, which is utilized in olfaction. In the olfactory epithelium, an individual odorant activates a diverse population of receptor neurons, and any individual receptor neuron can be activated by multiple odorants; it is the combination of activated neurons, rather than the class or location of individual receptor neurons, that constitutes the initial odor signal (Buck and Axel, 1991, Mombaerts et al., 1996, Malnic et al., 1999, Mori and Sakano, 2021, Endo and Kazama, 2022, Dikeçligil and Gottfried, 2024). Combinatorial coding provides far greater discriminatory power than labeled line coding. The olfactory system can distinguish upwards of a million distinct odors (Bushdid et al., 2014), while the gustatory system can only discriminate a handful of different tastes (Yarmolinsky et al., 2009, Barretto et al., 2015, Roper and Chaudhari, 2017), relying on olfaction to provide the perception of distinct flavors in the food we eat. The initial steps in olfactory coding are relatively well studied, with each olfactory receptor neuron expressing 1-2 olfactory receptors (Buck and Axel, 1991, Mombaerts et al., 1996). Inputs from olfactory receptor neurons expressing the same receptor converge on single glomeruli in the olfactory bulb, and the glomeruli project to higher processing centers such as the piriform

cortex (Blazing and Franks, 2020). However, much less is known about how these higher centers decode the combinatorial sensory signals to generate perceptions and physiological responses.

We have turned to *C. elegans* to study the downstream processing of olfactory combinatorial codes. The small size of the *C. elegans* nervous system and the availability of techniques for pan-neuronal activity recording now make it possible to study the neural basis for sensory-driven behaviors at whole-network scale in this model (Schrödel et al., 2013, Prevedel et al., 2014, Kato et al., 2015, Nguyen et al., 2016, Kotera et al., 2016, Venkatachalam et al., 2016, Nichols et al., 2017, Toyoshima et al., 2020, Hallinen et al., 2021, Yemini et al., 2021, Dag et al., 2023), as a foundation for understanding more complex nervous systems. Olfaction in *C. elegans* has classically been viewed as a labeled-line coding system rather than a combinatorial system, where specific subsets of chemosensory neurons respond to attractive odorants and drive positive chemotaxis (AWC, AWA), or respond to repulsive odorants and drive negative chemotaxis (AWB, ASH, ADL) (Bargmann et al., 1993, Troemel et al., 1997, Chao et al., 2004, Yoshida et al., 2012, Greene et al., 2016, Rengarajan and Hallem, 2016, Ferkey et al., 2021). However, recent observations challenge this view, as individual odorants have been shown to activate multiple classes of sensory neurons simultaneously, and individual olfactory neurons respond to a wide range of odorants (Lin et al., 2023). This arrangement is the hallmark of a combinatorial coding-based system, even though there are many fewer chemosensory neurons in *C. elegans*, and these neurons, individually, express many more olfactory receptors than their mammalian counterparts.

We have performed an in-depth analysis of one odorant, 1-octanol, which is encoded combinatorially (Lin et al., 2023), and is well-known to stimulate aversive behavior (Bargmann et al., 1993, Troemel et al., 1995, Troemel et al., 1997, Ferkey et al., 2021). We show that 1-octanol stimulation concurrently activates two separate and opposing sensory afferent pathways in the nervous system. These pathways converge to control at least four aspects of locomotion at the behavioral and circuit levels, with the balance between attraction and repulsion emerging as the critical factor determining the overall behavioral output. Furthermore, this coding strategy provides a simple framework to modulate sensory-driven responses to produce context-appropriate behavior.

Results

1-octanol repulsion in microfluidic arenas

1-oct avoidance in *C. elegans* has been intensively studied because it is strongly modulated by nutrition state and monoamine/neuropeptide signaling cascades (Chao et al., 2004, Wragg et al., 2007, Hapiak et al., 2013, Zahratka et al., 2015, Williams et al., 2018, Debnath et al., 2022). Our goal was to investigate the network basis of 1-oct repulsion using the NeuroPAL system (Yemini et al., 2021), which allows simultaneous whole-brain Ca^{++} imaging with unambiguous neuronal identification, coupled with quantitative analysis of 1-oct aversive behavior. 1-oct has previously been utilized as a volatile stimulus (Troemel et al., 1997, Chao et al., 2004), or in a gradient on agar plates (Khan et al., 2022, Fryer et al., 2024), while NeuroPAL recordings are performed in aqueous solution in microfluidics chips under confocal microscopy (Yemini et al., 2021). To better match the conditions for NeuroPAL recordings and behavioral

assays, we first investigated 1-oct repulsion in microfluidics arenas (Lockery et al., 2008, Albrecht and Bargmann, 2011, Lagoy and Albrecht, 2015), which gave us precise control over the concentration and spatio-temporal characteristics of the 1-oct stimulus. Using a simple two-chamber arena (Fig. 1A), we demonstrated that worms were repelled by a saturating concentration of 1-oct in S-basal (2.2 mM, corresponding to a 3.75 x 10^{-4} dilution; Fig. 1B-D). In our initial trials, we added 0.01% w/v xylene cyanol (0.1 mg/mL) to the 1-oct solution to visualize the interface between the stimulus and control buffer. However, as another study reported (Lagoy and Albrecht, 2015), worms were significantly attracted to xylene cyanol introducing an unwanted stimulus into the assays. We therefore optimized methods to maintain a stable interface between odorant and buffer chambers without the need for dye (see Methods). We assayed worms between 20 and 40 minutes after removal from food, during area-restricted search behavior (Gray et al., 2005), and calculated average chemotaxis indices (CIs) between 30 and 40 minutes (see Methods, and Fig. 1D, E). The -0.7 CI observed in the experiment shown represents strong repulsion.

Network-wide response to repulsive olfactory stimulation

To investigate the neuronal basis for the observed 1-oct aversive behavior, we performed network-wide Ca^{++} imaging during 1-oct stimulation, and identified the responding cells by imaging the neuronal landmarks encoded by the NeuroPAL fluorescent reporters (Fig. 2A). Worms were immobilized in 'olfactory' microfluidics chips (Chronis et al., 2007) for microscopy. Previous whole-brain studies have shown that certain neurons undergo spontaneous transitions between low and high activity states correlating with spontaneous reversals during foraging,

notably the reverse command neurons AVA, AVE, AVD, AVB, and the RIM neuron (Gordus et al., 2015, Kato et al., 2015, Nichols et al., 2017, Katz et al., 2019, Wirak et al., 2022, Sordillo and Bargmann, 2021, Li et al., 2023, Meng et al., 2024). We therefore used a recording/stimulus protocol consisting of a 6 min pre-stimulus period, followed by 6 30s applications of 2.2 mM 1-oct, spaced 30s apart, to help distinguish between spontaneous transitions and potential sensory-evoked transitions within this neuronal population. We observed dynamic activity patterns in dozens of neurons before and during 1-oct stimulus (Fig. 2B-D). Consistent with previous studies, AVA, along with AVE, AVD, RIM, AIB, and AIZ showed spontaneous state transitions, with the AVB forward command interneuron and the AIY interneuron showing mirror image patterns (i.e. AVB/AIY inactivated when AVA activated and vice versa). Typically, 3-4 transitions were observed in a 12 minute recording. These transitions took place during both the pre-stimulus and stimulus periods (Fig. 2D, 3A), and showed no obvious relationship with 1-oct application or withdrawal.

Sensory signals were also prominent, in both amphid and non-amphid chemosensory neurons. ASH and BAG showed strong consistent responses correlating with stimulus onset ('ON' responses). AWB also showed an ON response but also had high levels of spontaneous activity. ADL showed a strong ON response to the initial stimulus but was strongly desensitized in subsequent applications (Fig. 2D and 3B). ASH, AWB, and ADL were previously identified as the main neurons mediating 1-oct aversive responses (Troemel et al., 1997, Chao et al., 2004). 1-oct responses were also observed in AWA, ASE, ASK, ASJ, and URX (Fig. 2D, 3B), consistent with the observation of Lin et al, showing that 1-oct activates sensory neurons promiscuously

(Lin et al., 2023). Significantly, we observed a strong 1-oct response in AWC neurons (both AWC^{OFF} and AWC^{ON}; Fig 2-D, 3B). AWC activity decreased upon 1-oct addition and rebounded upon 1-oct withdrawal, in a typical 'OFF' neuron pattern (Chalasani et al., 2007), opposite to ASH (Fig. 2B-D, 3C). This was surprising, first, because AWC is usually considered an attractive neuron, not expected to respond to a repulsive odorant, and second, because the observed AWC pattern predicts that AWC should drive attraction to 1-oct (Chalasani et al., 2007, Im Choi et al., 2018, Ferkey et al., 2021, Khan et al., 2022). 1-oct has thus far only been described as a repellent for *C. elegans*, with no attractive properties (Bargmann et al., 1993, Chao et al., 2004, Ferkey et al., 2021, Fryer et al., 2024). Strong sensory-driven activity was also observed in AIA and SAA interneurons, suggesting these two neurons may receive substantial inputs from the sensory neurons (Fig. 2D, 3C). Apart from AIA, the other 'first layer' interneurons AIB, AIY, and AIZ did not show detectable sensory-driven activity (Fig. 3A), despite their extensive anatomical connections with sensory neurons, suggesting these interneurons may be receiving their principal functional inputs from elsewhere in the circuit.

To better understand how sensory inputs may pattern global network activity patterns, we performed correlation analysis on selected data sets in which we were able to identify 12 key neurons with well characterized roles in sensory motor coupling (Gray et al., 2005, Chalasani et al., 2007, Ferkey et al., 2021). To detect the sensory signature, we compared neuronal correlation patterns in the first 6 minute interval (prior to stimulation), and the second 6 minute interval (where stimulus was applied and removed for alternating 30s periods) (Fig. 3E). We observed the expected increases and decreases in correlation among the sensory neurons (i.e.

ASH and BAG became correlated, and anti-correlated with AWC). We did not observe any increased correlation between the motor command interneurons and sensory neurons, consistent with the absence of a consistent relationship between state transitions and 1-oct application. However, the degree of activity cross-correlation among AVA, AVE, AVD, AIB, and RIM was increased during the stimulus period, and AIB also showed increased correlation with ASH. These observations suggest that sensory information was penetrating to the locomotory command circuit level even if there was no obvious sensory entrainment of the principal neurons in those circuits (Fig. 3D, E).

Finally, we observed several neurons with activity patterns which did not correspond to the locomotory command group or the sensory-dependent group, which included SMDV, RIA, and RMDD (Fig. 2D), which are generally associated with turning behavior (White et al., 1986, White, 2018, Ouellette et al., 2018), indicating that 1-oct exposure may also bias the locomotory heading as well as reversal frequency.

The balance of simultaneous repulsion and attraction shapes the chemotactic response

The observation that 1-oct application and withdrawal cycles activate ASH and AWC in alternation predicts that these two neurons generate antagonistic inputs into the locomotory circuitry. Specifically, ASH activity varies in phase with 1-oct application, predicted to stimulate in-phase reversal consistent with a repulsive chemotactic response. AWC activity varies out of phase with 1-oct application, predicted to inhibit in-phase reversals and stimulate out of phase reversals, consistent with an attractive chemotactic response. This puzzling activity pattern led

us to hypothesize that 1-oct is encoded combinatorially, simultaneously as a repellant (by ASH) and an attractant (by AWC), and these two afferent pathways balance one another during the application-withdrawal cycle, and mutually antagonizing sensory entrainment of the reverse command neurons and potentially attenuating 1-oct behavioral responses.

To test this hypothesis, we selectively inhibited repulsive inputs to unmask latent effects of the attractive inputs and vice versa. To manipulate repulsive inputs, we reduced the 1-oct concentration. Recently, Lin et. al. (2023) reported 1-oct concentration-response relationships for ASH and AWC. At sub-saturating concentrations, ASH responses were highly concentration dependent while AWC 'ON' responses were relatively insensitive to concentration. First, we repeated the observations of Lin et al., extending the concentration range to saturation (2.2mM, shown to be repellent in microfluidics-based assays; Fig. 1), recording ASH responses, and both the AWC 'ON' and 'OFF' responses. We serially stimulated worms with 0.22 mM, 0.66 mM, and 2.2 mM 1-oct. ASH responses showed significant concentration-dependent increases, whereas AWC 'ON' and 'OFF' responses did not (Fig. 4A-C). Behaviorally, after 3- and 10-fold dilution, the 1-oct response switched from repulsion to attraction (Fig. 4D), while 1.4 to 2.0-fold dilutions attenuated chemotactic responses (Fig. 4D), potentially reflecting a more even balance between the two signaling pathways. This result suggests that ASH-mediated repulsive inputs dominate AWC-mediated attractive inputs at saturating concentrations, causing overall repulsion, but as ASH input strength decreases relative to AWC in progressively more dilute 1-oct, AWC attractive inputs come to dominate, causing attraction.

We then used a genetic approach to manipulate attractive inputs. Sensory signal transduction in AWC but not ASH is eliminated in *tax-4* mutants, which lack a cGMP-gated ion channel downstream of sensory receptors (Coburn and Bargmann, 1996, Wojtyniak et al., 2013, Ferkey et al., 2021, Taylor et al., 2021). Loss of TAX-4 converted 1-oct back to a repellent at the lower concentrations (Fig. 4C), indicating that TAX-4 signaling is clearly contributing to 1-oct chemotactic responses in this context. Similarly, at saturating concentrations, we observed a trend toward increased repulsion, although this observation did not rise to statistical significance because of high variability in the CI values. Overall, these experiments support the idea that 1-oct is encoded as multiple parallel inputs with opposite valence, operating concurrently. The ASH inputs promote repulsion while the AWC inputs promote attraction, and the balance of their relative strengths dictates the final chemotactic outcome (Fig. 4E).

To understand the interaction of these co-activated afferent pathways at the level of locomotory decision making, we closely examined the behavior of worms as they encountered the interface between 1-oct solution and control buffer in microfluidic devices. We began using the microfluidics 'stripe' chip (Albrecht and Bargmann, 2011, Lagoy and Albrecht, 2015), containing a central zone of 2.2 mM 1-oct flanked by zones containing control buffer, and we used automated tracking (Itskovits et al., 2017) to quantify the relative prevalence of reversals, a key component of klinokinesis-based chemotaxis (Gray et al., 2005), upon entering or leaving the 1-oct zone, compared to successful transits across the zone boundary (Fig. 5A, B). Surprisingly, for worms entering the 1-oct zone, entry transits outnumbered entry reversals by nearly 2:1 (Fig. 5B, C). In *osm-9* mutants, in which the 1-oct responses of ASH are defective

(Colbert et al., 1997, Ezak et al., 2010, Zahratka et al., 2015), the ratio was skewed significantly toward entry transits, demonstrating that OSM-9 signaling promotes 1-oct avoidance. Interestingly, in *tax-4* mutants, the ratio was strongly skewed toward entry reversals. This result indicates that *tax-4* signaling actively suppresses 1-oct avoidance, consistent with its role in promoting 1-oct attraction (Fig. 5B, C). This attraction-promoting role was also observed for worms exiting the 1-oct zone (Fig. 5B, D). Here, exit reversals strongly outnumber exit transits. These reversals are dependent upon TAX-4, but do not require OSM-9 (Fig. 5D). These observations confirm that TAX-4 mediated attractive signaling significantly shapes the behavioral response to 1-oct, despite the fact that 1-oct is classified as a strong repellent. Most importantly, it highlights how overall chemotactic behavior is reciprocally regulated by two different locomotory transitions (reversals due to increased d[1-oct]/dt and reversals due to decreased d[1-oct]/dt), and how two opposing sensory afferent pathways converge to regulate a single locomotory transition, namely reversals due to increased d[1-oct]/dt, at a single point in time and space (Fig. 5B).

These behavioral data raised a new important question: how can wild-type worms avoid the 1-oct containing zone when their reversal decisions favor entry and retention? We had noticed that contact with 2.2 mM 1-oct caused worms to rapidly and reversibly increase their locomotory activity, suggesting an additional potential mechanism in play. To quantify this effect, we measured the average distance worms moved when we flooded the microfluidics arena with 2.2 mM 1-oct, comparing the distances traveled in a 2-minute interval in control buffer and 1-oct. Worms significantly increased their locomotion in 1-oct, and returned to

baseline rates 2-4 minutes after 1-oct withdrawal (Fig. 5E). Next, we created a simple behavioral simulation to determine whether this selective increase in locomotory activity could counteract the observed bias in reversal probabilities to achieve overall avoidance. The environment was modeled as a line divided into two equal compartments, representing the control buffer and the 2.2 mM 1-oct halves of the arena. Worms were modeled as one-dimensional particles, free to move along the full length of the line. They were allowed to reverse direction at random along the length of the line, but were specified to reverse direction with fixed probabilities at the buffer/octanol interface, depending on which direction they approached from. Finally, the particles moved at different relative rates in the buffer and 1-oct compartments (Fig. 5F). Using our measured entry and exit reversal probabilities as inputs, this simulation showed that relative locomotory speed is a critical factor determining overall chemotaxis behavior, with a 60% speed increase sufficient to convert attraction to repulsion, given our observed interface reversal probabilities (Fig. 5F). This simulation was highly simplified, and did not take into account the persistence of higher locomotion speeds once worms exited 1-oct (Fig. 5E), which could further potentiate repulsion since faster-moving exiting worms will be oriented away from the 1-oct zone, biasing their trajectories toward the further reaches of the buffer zone where they eventually slow. Importantly, these results extend the idea that 1-oct is encoded combinatorially, generating a sensory signal with at least three components: 1) promotion of reversals when encountering increased [1-oct], 2) promotion of reversals when encountering reduced [1-oct], and 3) increase of locomotory speed when encountering increased [1-oct]. These three modalities engage differentially at different concentrations, and are ultimately integrated to determine the final chemotactic outcome.

Repulsive and attractive signaling competitively entrain the locomotory command neurons

To understand how the repulsive and attractive 1-oct signals affect locomotory reversals, we examined the activity pattern of the AVA reverse command interneuron in relation to 1-oct addition and withdrawal. First, it was necessary to develop a data analysis approach to detect and quantify sensory-driven patterns of AVA activation, given the well-documented patterns of spontaneous AVA activity state transitions (Gordus et al., 2015, Kato et al., 2015, Nichols et al., 2017, Katz et al., 2019, Wirak et al., 2022, Sordillo and Bargmann, 2021, Li et al., 2023, Meng et al., 2024) that could potentially obscure a sensory signal. To reduce the impact of these transitions, we averaged at least 6 recordings of AVA activity for each condition tested so that non sensory-associated AVA transitions would tend to average out with larger numbers of recordings, akin to spike-triggered averaging (De Boer and Kuyper, 1968, Bryant and Segundo, 1976, Davidson et al., 2007). We then calculated the 'entrainment index' (EI), as a measure of how strongly a response is positively or negatively correlated with 1-oct application, and quantified the probability that an observed correlation is greater than a random association (see Methods), setting a threshold of $P<0.05$ for non-random association. To validate this test, we analyzed ASH and AWC responses to 1-oct application, which were obviously highly correlated and anti-correlated, respectively. The ASH and AWC EIs showed the expected positive and negative values (Fig. 6A), with $P <0.0015$, indicating a less than one in six hundred chance that the correlations in neuronal responses with 1-oct applications were random (Fig. 6B). Applying this test to AVA activity, we observed strong inverse correlation with stimulant application at 0.22 mM 1-oct (the lowest tested concentration), and a significant negative EI value (Fig. 6C, D, H). This concentration was attractive, and showed the lowest ASH:AWC activity

ratio (Fig. 4), suggesting that AWC may be driving AVA with minimal interference from ASH. At higher [1-oct] (0.66, 2.2 mM), AVA entrainment with 1-oct application were shifted positively to a large extent (compared to 0.22 mM; Fig. 6C, D, H), and were not significantly different from random (P>0.05). At these concentrations, the ASH:AWC activity ratio is significantly increased (Fig. 4), consistent with the idea that a lack of entrainment may reflect interference between AWC and ASH signals impinging on AVA.

To further support the idea that conflicting sensory signals may mask one another at the level of AVA, we measured EIs in TAX-4 animals. At the lowest [1-oct], the strong negative entrainment previously observed was abolished, confirming that negative entrainment is a function of TAX-4 signaling (Fig. 6E, F, H). At the intermediate [1-oct] (0.66 mM), *tax-4* loss of function mutation caused a slight positive shift in the EI, but did not lift it above the threshold for significant entrainment (P>0.05) (Fig. 6E, F, H). However, at the highest [1-oct], loss of TAX-4 positively shifted the EI into the significant range for positive entrainment (Fig. 6E, F, H). Interestingly, all of the calculated AVA EIs (Fig. 6H) correlate well with the overall chemotactic behavior in terms of sign (i.e negative entrainment predicts attraction, positive entrainment predicts repulsion), even where the strength of entrainment with the sensory input did not exceed our set threshold for non-random entrainment (see Discussion). Most importantly, these results imply that the reverse command interneurons under these assay conditions will not necessarily show overt entrainment to sensory stimuli even though they are receiving sensory inputs because sensory stimuli may be encoded as parallel antagonistic afferent inputs

which cancel one another out, until the prevailing conditions permit one input to become substantially stronger than the other.

To investigate how the 1-oct sensory signals are transmitted to AVA, we examined the interneuron AIB, which is positioned to be an integrating hub in this system because it receives afferent inputs from ASH and AWC, and many other sensory neurons, and makes strong connections with the reverse and forward command interneurons. AIB also receives inputs from RIM, which provides feedback about the motor state that is used in the regulation of sensory afferent pathways by corollary discharge (Gordus et al., 2015, Ji et al., 2021, Riedl et al., 2022). Initially, we did not observe significant entrainment of AIB activity with 2.2 mM 1-oct application (Fig. 6G). A potential reason might be that motor feedback was obscuring the sensory signal. To address this possibility, we subtracted AVA activity, representing the motor state, from the AIB activity. This modified AIB signal showed significant entrainment with 2.2 mM 1-oct application which was positive in sign (Fig. 6 G and H), and greater than AVA's entrainment at the same 1-oct concentration. These observations suggests that AIB serves as a sensory relay for the aversive inputs, but since aversive entrainment in AVA is weaker than that in AIB (presumably due to interference from attractive inputs), the site of integration between repulsive and attractive pathways must be downstream of AIB and either at or upstream of AVA.

Combinatorial olfactory coding facilitates context-dependent behavioral flexibility

What benefit might *C. elegans* gain from encoding 1-oct combinatorially, simultaneously activating attractive and repulsive afferent input pathways? This strategy could create a simple

and versatile mechanism to modulate the behavioral output to best match internal and external conditions, such as specific odorant concentration, the presence of other odorants, or interoceptive inputs such as hunger or stress. A combinatorial strategy allows response sensitivity and even valence to be altered by simply adjusting gains or synaptic outputs within each pathway (Fig. 7A), without requiring extensive functional reorganization of the downstream connections, or recruitment of complex cross-inhibitory circuitry. For example, in the laboratory, 1-oct is used as a repellant for *C. elegans*, but its presence in the environment may convey more complex information. 1-oct is toxic to worms, which presumably explains why *C. elegans* has evolved to avoid it, at least at higher concentrations. However, 1-oct is naturally found in decaying plant material (Bourgou et al., 2012, Neelakandan et al., 2021), so it may also signal the presence of a bacterial food source for worms. In the presence of non-toxic alternatives, other food sources are safer, but in the absence of alternatives, worms may risk toxicity to avoid starvation. Could combinatorial coding support the risk-reward decision making required of *C. elegans* when evaluating environmental 1-oct signals? Consistent with this idea, many attractive food signals, including isoamyl alcohol (IAA), suppress AWC activity (Chalasani et al., 2007, Yoshida et al., 2012, Lin et al., 2023), and could therefore decrease the activity of the attractive afferent pathway to disinhibit repulsion (Fig. 7A, B). We tested this hypothesis by conducting chemotaxis experiments at 0.66 mM 1-oct, normally an attractive concentration in our microfluidics assays, in the presence of isoamyl alcohol (IAA, 10^{-4} dilution, added to both the 1-oct and control buffer sides of the microfluidics arena). Under these conditions, worms were strongly repelled by 1-oct (Fig. 7C). The probability of reversals when entering the 1-oct zone was increased (Fig. 7D), the probability of reversals when exiting the 1-

oct zone was decreased (Fig. 7D), and the repulsion-inducing modulation of locomotory speed was also increased (Fig. 7E, F). Interestingly 0.66 mM 1-oct did not cause a speed increase on its own (unlike 2.2 mM, Fig. 5). Acute application of IAA also did not affect speed. However, 0.66 mM 1-oct in the presence of IAA caused a large speed increase (2-fold). Since IAA reduces AWC activity, this IAA effect may be due to removal of AWC inhibition of 0.66 mM 1-oct-dependent speed modulation. These three quantitative changes in locomotory parameters will each shift the chemotaxis index in the negative direction, converting 1-oct attraction to repulsion.

In network recordings, the presence of IAA greatly increased the sensory entrainment of AVA, positively correlating with stimulus application. This effect was observed at 0.66 mM (Fig. 7G, H) and 2.2 mM 1-oct (not shown), suggesting that IAA will potentiate 1-oct avoidance by klinokinesis, or in other words, increasing the probability that worms will execute a reversal when they experience positive d[1-oct]/dt. These results provide proof-of-principle that rebalancing of the afferent input pathways to reduce attraction and promote repulsion can control chemotaxis in an ethologically relevant manner, and demonstrate the potential utility and flexibility of the combinatorial coding strategy.

Discussion

We have investigated the response of *C. elegans* to the odorant 1-oct, using a combination of microfluidics-based behavioral analysis and whole-network Ca^{++} imaging. Ca^{++} imaging using the NeuroPAL system (Yemini et al., 2021) showed that 1-oct activates at least 11 different sensory neurons including neurons associated with chemorepulsion and

chemoattraction. Paradoxically, 1-oct activates the ASH and AWC sensory neurons, with ON- and OFF- response kinetics, respectively. This pattern indicates that, upon both 1-oct onset and offset, sensory signals are being generated to simultaneously promote and inhibit locomotory reversals. Based on this observation, we hypothesized that 1-oct may be encoded as two simultaneous and opposite afferent pathways: a repulsive pathway driven by ASH and possibly other neurons, and an attractive pathway driven by AWC and possibly other neurons, with the ultimate chemotactic outcome determined by the balance between the two. We tested this hypothesis by altering the balance between the pathways. This goal was achievable by simply changing the 1-oct concentration, because the ASH 1-oct response was highly sensitive to concentration while the AWC 1-oct response was not. At the highest 1-oct concentration tested (saturation, 2.2 mM), worms were repelled by 1-oct in microfluidics-based assays where worms were given the choice between control buffer or buffer containing dissolved 1-oct. However, 3-fold and 10-fold dilutions of 1-oct were attractive, presumably because the ASH-driven repulsive pathway was weakened while the AWC-driven attractive pathway remained strong. Consistent with this interpretation, the attraction could be eliminated by mutating TAX-4, a critical component of sensory signal transduction in AWC. Worms achieved these chemotactic outcomes by modulating at least three distinct locomotory transitions (Fig. 8A): reversals stimulated upon entering the 1-oct zone, reversals stimulated upon exiting the 1-oct zone, and modulation of locomotory activity within the 1-oct zone (i.e. locomotory speed). Based on numerical simulations, speed modulation was the most important factor: reversal patterns at the highest 1-oct concentration clearly favored attraction but increased locomotory activity within the 1-oct zone overcame this bias and caused repulsion. Input from the two

hypothesized pathways strongly overlapped in their regulation of the locomotory transitions (Fig. 8A). Reversals upon entry were reduced in *osm-9* mutants, implying they may be stimulated by ASH, but increased in *tax-4* mutants, implying they may be inhibited by AWC. Reversals upon exit were reduced in *tax-4* mutants, suggesting they are stimulated by AWC (we did not observe reciprocal regulation by OSM-9/ASH). Speed modulation, like ASH activity, was dependent on 1-oct concentration (observed in wild type worms only at the highest 1-oct concentration). However, IAA addition, which suppresses AWC activity, unmasked strong speed modulation at a lower 1-oct concentration, suggesting that the AWC-driven pathway may inhibit 1-oct dependent speed increase by counterbalancing the ASH-driven pathway. Our findings provide consistent support for the idea that 1-oct is encoded simultaneously as two opposing afferent pathways which reciprocally modulate multiple locomotory parameters to influence overall chemotactic behaviors (Fig. 8A). However, it remains necessary to identify the specific sensory neurons that contribute to these respective pathways to further support this view of sensory coding in the *C. elegans* olfactory system.

Our results and those of Lin et al (Lin et al., 2023) demonstrate the capacity of *C. elegans* to utilize combinatorial coding to perceive and respond to olfactory stimuli. Until recently, labeled line olfactory coding has been the predominant paradigm in *C. elegans* olfaction, where odorants are considered to be either repellants or attractants (i.e. positive or negative valence), activating either repulsive or attractive sensory neurons and repulsive or attractive downstream pathways (Fig. 8B, (Troemel et al., 1997, Tsunozaki et al., 2008, Yoshida et al., 2012, Ferkey et al., 2021). However, this framework is incompatible with findings that individual odorants

simultaneously activate multiple sensory neurons associated with both valences, because the labeled line framework has no provision for integrating conflicting inputs. Lin et al (Lin et al., 2023) showed that individual odorants activated a wide range of amphid neurons associated with both valences, and that individual sensory neurons were activated by many different odorants. Thus, in *C. elegans*, like in insects and vertebrates, the initial representation of an odorant may be formed by the identities and relative activity levels of a population of olfactory neurons. It remains poorly understood, in any system, how this initial representation is processed downstream to inform physiological and locomotory responses. Our results suggest that the initial code may represent multiple independent afferent pathways, those pathways may be antagonistic, and they behave like labeled lines independently controlling multiple locomotory parameters which make up the overall chemotactic response. While previous work in *C. elegans* has shown that antagonistic sensory inputs can contribute to chemosensory responses (Hukema et al., 2006, Jang et al., 2012, Murayama and Maruyama, 2013, Ghosh et al., 2016), this study is the first to show in detail how multiple olfactory inputs interact to shape chemotactic outcomes at the behavioral and circuit levels. Interestingly, a labeled line-like olfactory response was also observed in mammals, where optogenetic stimulation of a single olfactory glomerulus in transgenic mice elicits one of the locomotory components (freezing) which make up a complex olfactory-stimulated fear response (Saito et al., 2017). However, more complex coding mechanisms are probably also utilized, since olfactory codes representing multiple odorants show synergistic recruitment of olfactory neurons, and cross-inhibition among olfactory neurons is common (Horio et al., 2019).

The compact size of the *C. elegans* nervous system makes it feasible to characterize at a cellular and molecular level where and how these afferent pathways converge and interact to pattern overall behavior. We found that the two afferent pathways behave like separate labeled lines extending from the sensory level all the way to the level of the AVA locomotory command interneurons, which drive locomotory reversals (Chalfie et al., 1985, Piggott et al., 2011), thereby connecting the afferent pathways directly to behavior. AVA activity patterns integrate the two afferent pathways (Fig. 8A), but this responsiveness was often difficult to detect because of the antagonism between the pathways, on top of the stochastic transitions that AVA (and other command interneurons) undergo between low and high activity states. Because AVA sensory entrainment varies smoothly as a function of the relative activity levels of the two pathways, the pathways probably do not strongly cross-inhibit one another, but act in a more additive manner. Cross-inhibition would likely result in a much steeper transition in AVA entrainment from the attractive to the repulsive pathway as the balance shifts, akin to the effect of cross inhibition between left and right lateral superior olive (LSO) neurons (via the medial nucleus of the trapezoid body) in the mammalian sound localization circuitry (Grothe et al., 2010). There, either the left or the right LSO will be active as a function of the horizontal position of the audio source, but cross-inhibition prevents both being active at the same time.

How are the repulsive and attractive pathways integrated to produce the final behavioral outcome? Careful examination of the circuitry at multiple 1-oct concentrations, with targeted manipulations of sensory neurons and interneurons will be needed to fully answer this question, but the activity patterns of AIB provide some initial insights. AIB is a first layer

interneuron that receives extensive inputs from sensory neurons including ASH and AWC, strong synaptic inputs from other first layer interneurons (AIZ, AIA), and electrical and chemical synapses from locomotory command neurons AVE and RIM; AIB sends projections back to the locomotory command neurons including AVA, RIM, and AVB (White et al., 1986, Witvliet et al., 2021). Based on this connectivity, AIB is positioned as an integrating hub for primary sensory inputs, processed sensory inputs, and locomotory state information, and it strongly influences locomotory state transitions (Wang et al., 2020). As such, AIB is ideally positioned to integrate the attractive and repulsive afferent pathways and relay that information to AVA. Prior to sensory stimulation, AIB activity followed reverse command interneuron activity, as has been observed previously (Gordus et al., 2015, Kato et al., 2015). Upon stimulation, AIB became significantly more correlated with ASH based on global correlation analysis, but its entrainment index did not show significant association with odorant application. However, once the noise from locomotory state transitions was subtracted, strong positive AIB entrainment with 1-oct application could be seen. Surprisingly, this entrainment suggests that AIB relays repulsive afferent information to AVA, rather than playing an integrating role that is more in line with its synaptic connectivity profile. Unlike AIB, AVA is not significantly entrained positively or negatively to stimulation in these same recordings, perhaps because co-incident and opposite inputs coming from the attractive afferent pathway obscure the entrainment. This finding therefore implies that the point of integration is AVA itself or a different presynaptic partner that also receives AIB inputs. Possible routes for the attractive afferent information to reach AVA are not obvious based on the connectome and our data. Because AWC makes only a single synapse on AVA (White et al. 1986), the route is most likely indirect. AWC makes extensive

synapses onto AIA and AIB, and AIA synapses onto AIB, but this possible route is not supported because AIB is positively entrained to stimulus, opposite of the AWC activation pattern. Interestingly, AIA activity positively correlates with AWC in this study, suggesting they are connected by excitatory (sign preserving) synapses, but in other studies using IAA as a stimulus, AWC drives AIA activity via sign-inverting inhibitory synapses (Chalasani et al., 2010). AIA expresses both inhibitory and excitatory glutamate receptors (Hammarlund et al., 2018), and it will be interesting to determine why AIA responds differentially to AWC depending on which odorant is used as the stimulus. Another possible source of input to AVA is SAA. SAA also shows a strong positive correlation with AWC in our recordings, and SAA makes more synaptic connections than any other neuron onto AVA and, likewise, onto RIM. Reinforcing this connection, AVA and RIM are also connected by gap junctions. Therefore, SAA is a strong candidate to provide AVA with input from the attractive input afferent pathway. However, the connectome does not identify synaptic inputs to SAA that are related to 1-oct sensation in any obvious way. The only direct sensory inputs to SAA are the oxygen sensing neurons PLN and ALN, and the mechanosensory neurons DVA and ADE. The sources of input to and functional significance of SAA will require further study.

The novel aspect of the coding strategy proposed here is that it relies on two separate antagonistic circuits which are stimulated by the same odorant and operate concurrently, becoming integrated deep in the sensory motor circuitry to determine the ultimate behavioral output. Other examples of behavioral plasticity in *C. elegans* involve switching between two different circuits, one attractive and one repulsive. The switch may happen at or near the

sensory level or at deeper levels (Tsunozaki et al., 2008, Yoshida et al., 2012, Ha et al., 2010, Khan et al., 2022), but regardless, the attractive and repulsive circuits do not operate concurrently. Here, we present the first evidence that both overall chemotactic behavior and the sensory entrainment of AVA are reflective of two pathways providing opposite inputs simultaneously, because weakening one pathway reveals the presence of the other across a broad concentration range. This coding strategy potentially provides a simple and versatile mechanism for generating olfactory plasticity. By analogy with the refraction of light through two prisms (Fig. 8C), the chemosensory neuron array in *C. elegans* creates a multi-factorial representation of the sensory stimulus, (i.e. the first prism), differentiating inputs from multiple sensory neurons, each with different downstream behavioral correlates. Downstream, the different components of this representation will eventually converge and become integrated into a coherent behavioral response by the motor command circuitry (i.e. the second prism). Because the sensory neurons have different concentration-response profiles, worms can easily generate differential behaviors dependent on stimulus concentration: as concentration is reduced, the input from the sensory layer will be skewed toward the higher-affinity components and away from the low-affinity components (Fig. 8C). In this study, reduced [1-oct] favored the AWC-driven response (higher affinity) over the ASH-driven response (lower affinity), converting the 1-oct response from repulsion to attraction. This architecture also provides versatile avenues for modulation. Multiple sensory inputs may be integrated if the additional odorants modulate the initial sensory representation, either additively (via ON neurons) or subtractively (via OFF neurons Fig. 8C). Here, addition of IAA restored repulsion at lower concentrations by reducing the contribution of AWC. In the two prism analogy, IAA is equivalent to a selective

optical filter placed in the light path, skewing the overall balance back toward ASH. Other forms of plasticity may also be easily incorporated into this scheme. For example, monoamine or neuropeptide modulation could affect sensitivity or valence of olfactory responses by selectively increasing or decreasing the excitability of sensory neurons or interneurons within the component pathways. Similar adjustments to the relative strengths of the pathways could also be utilized to effect experience-dependent plasticity. In a complex natural environment where multiple odorants, interoceptive inputs, and experience-dependent plasticity are all acting at the same time to shape a worm's locomotory decisions, it may be advantageous to funnel all of the modulatory influences through one major repulsive pathway and one major attractive pathway so they will act additively and influence the final downstream integration instead of having all of the potential modulatory factors individually specifying downstream circuit switching, which, in a small nervous system, could create chaos as a large number of modulators compete to modulate the function of a finite number of downstream interneurons.

Materials and Methods

Worm maintenance and strains:

C. elegans were maintained at 20°C on NGM agar plates and fed *E. coli* OP50 bacteria. All experiments were conducted at 20-22°C (Brenner, 1974, Stiernagle, 2006). The following strains were utilized:

N2: *Wild-type.*

OH15500: otIs669 V, otIs672 [rab-3::NLS::GCaMP6s + arrd-4:NLS:::GCaMP6s](Yemini et al., 2021).

AML320: otIs669 V, wtfIs145 [rab-3p::his-24::GCaMP6s::unc-54 3' UTR + pBX].

VC3113: tax-4 (ok3771) III.

CX10: osm-9 (ky10) IV.

FY1041: tax-4 (ok3771) III, otIs669 V, wtfIs145 [rab-3p::his-24::GCaMP6s::unc-54 3' UTR + pBX].

Strains were obtained from the Caenorhabditis Genetics Center (CGC), funded by NIH (P40 OD010440). VC3113 was crossed into AML320 to generate FY1041. Homozygous TAX-4 mutants were genotyped by PCR and selected based on fluorescence. Strains were allowed for three generations of growth before experiments.

Microfluidics device fabrication and behavioral assays

All behavioral studies were conducted in microfluidic devices following standard protocols (Lockery et al., 2008, Albrecht and Bargmann, 2011, Lagoy and Albrecht, 2015). Devices were fabricated by thoroughly mixing polydimethylsiloxane (PDMS) and a curing agent in a 10:1 ratio by weight (Sylgard 184, Electron Microscopy Sciences Cat. 24236 – 10), degassing

the mixture under vacuum, and then pouring it onto a silicon mold at ~5 mm height. PDMS was cured by incubating at 65°C for at least 3 hours. Olfactory chips were obtained from Microkosmos (ukosmos.com).

Chemotaxis: Chemotaxis assays utilized a 'two-chamber' device dividing the arena into equal chambers for stimulus and control buffer (S-basal [100mM NaCl, 5mM g K_2HPO_4, 45mM KH_2PO_4, pH = 6]). Worm behavior was recorded using AmScope microscope cameras (MD 500, MU 500-HS, AmScope, Irvine, CA), and videos were processed using Adobe Premier Pro 2024 (Adobe Inc., San Jose, CA). 1-2 day old young adult animals were picked and washed with S-basal and loaded into the behavioral arena. Animals were acclimatized in the arena for 5 minutes, assays were performed between 20-40 minutes from starvation onset while they were in area-restricted search foraging mode (Gray et al., 2005). In the original microfluidics protocols (Albrecht and Bargmann, 2011, Lagoy and Albrecht, 2015) 0.01% w/v xylene cyanol (0.1mg/ml) dye was used to verify clean separation between different domains within the microfluidics device. However, worms show clear attraction to 0.01% xylene cyanol (data not shown) raising the question that presence of dye might introduce additional sensory activity. So, we modified the protocol to incorporate dye only before and after the assay instead of continuous use during the assay (Fig 1A). Using dye, we validated that arena configuration stays stable for up to 90 minutes. Using dye, we checked arena configuration before loading worms and after the assay was complete. If arena configuration was correct immediately before worm loading and immediately after assay completion (total 30 - 40 minutes period), we considered configuration to be stable in between. Assays that showed uneven configuration after completion were

excluded from analysis. Chemotaxis index was calculated between 10-20 minutes of stimulus onset, using the equation: Chemotaxis Index (CI) = (Number of worms in stimulus – Number of worms in buffer)/Total number of worms, positive and negative indices representing attraction and aversion respectively. Assays were repeated 3-5 times and analyzed by *Student's t-test*.

Distance traveled: Locomotory distance-traveled assays used the 'two-chamber' device with both chambers containing the same solution. Worms were exposed sequentially to buffer (5 mins), stimulus (5 mins), and buffer (10 mins). A complete exchange of solutions takes approximately 1 minute. Data was collected 90 seconds after solution change to ensure complete exchange. 2 minutes from the buffer phase (pre-stimulus), 2 minutes from the 1-oct phase (stimulus), and successive 2-minutes intervals after 1-oct withdrawal (post-stimulus) were analyzed to calculate the distance traveled per minute/worm in each condition. Worm tracks were manually traced and measured using Adobe Premiere Pro 2024 and Graphic for Mac (Autodesk, San Francisco, CA). Pooled data were analyzed by one-way ANOVA and Tukey's multiple comparisons post-analysis test. Worm locomotion simulation was written in Mathematica using AI-enabled chat (Mathematica, Princeton NJ, code available upon request). In the simulation, 20 one-dimensional dots, representing worms, were allowed to travel a one-dimensional line, representing behavior arena. The line was divided equally into two zones, representing buffer and stimulus, and dots moved freely within the line with random reversal frequency. Dot speed increased in the stimulus zone, as indicated, and reversal frequency at the interface was specified as observed from behavioral assays. 10 simulations were performed for each speed differential tested.

Reversals: Analyses of locomotory reversals were performed using larger 'stripe' chips (Albrecht and Bargmann, 2011), which provided a greater working area and facilitated automated video tracking by reducing the frequency of collisions between worms. These chips were usually configured with 3 zones of equal size: a stripe of 1-oct down the middle flanked on either side by buffer, although for some experiments, the 1-oct was placed on one side. Video recordings of worm behavior were analyzed using the Multi-Worm Tracker (Itskovits et al., 2018), using MatLab (Mathworks, Natick, MA), with manual analysis of individual tracks to quantify reversals. Assays were repeated 3 times, data were pooled and analyzed by *Fisher's exact test*.

Whole-brain calcium imaging:

Neuronal activity was examined by measuring calcium transients detected by fluorescence change (GCaMP6s, OH15500 (Yemini et al., 2021), AML320 (Yu et al., 2021)). Calcium imaging was conducted as previously described (Chronis et al., 2007, Gordus et al., 2015, Kato et al., 2015). Animals were anesthetized with 1 mM tetramisole hydrochloride (Sigma, CAS 16595-80-5) in S-basal buffer and imaged in PDMS olfactory microfluidic devices, which trap the worm in a chemical delivery system and provides inlets to deliver either buffer or stimulus to the nose using laminar flow (Chronis et al., 2007). Head-ganglia neurons were recorded using Leica confocal microscope (SP8) at 0.6 - 0.8 Hz rate. Odorants were diluted in S-basal. Each worm was recorded for 12-14 minutes within 20-40 minutes from starvation onset, starting with 6 minutes of buffer exposure followed by 6-7 30-second pulses of stimulus with 30-second intervals. Calcium imaging was followed by immediate recording of NeuroPAL color

markers. For +IAA experiments, IAA delivery to the nose was started at 5 minutes of recording, 1 minute before the first stimulus application, and IAA was added to both stimulus and buffer thereafter. For concentration-response of ASH and AWC experiments, three 0.22 mM, two 0.66 mM and two 2.2 mM 1-oct pulses were supplied serially; repeated application produced identical response amplitudes.

Recorded image files were stacked and analyzed using Fiji/ImageJ (Schindelin et al., 2012, Schneider et al., 2012) followed by motion correction with 'MoCo' plug-in (Dubbs et al., 2016). Neuron identity was manually assigned and matched with calcium response using guidelines described by Yemini and Hobert (Yemini et al., 2021). Neurons with ambiguous identities were excluded from the analysis (Fig. 2). Individual neuron activity was then normalized and re-sampled, before averaging, by 'Min-Max normalization' and 'Linear interpolation' respectively, using custom R-scripts (Kuramochi and Doi, 2017).

Data analyses and statistics:

Statistical analyses were performed using Prism v10.2.1 (GraphPad Software Inc., La Jolla, CA), R v4.3, R-Studio v2022.07.1 (Posit PBC, Boston, MA), MatLab vR2023A (MathWorks, CA) and Microsoft Excel 2016.

Averaged calcium responses were used to calculate Entrainment index (EI). EIs were calculated by adding the six individual 30s Area Under Curves (AUC) corresponding to each stimulus application. To evaluate the significance of EI, sums of 6 randomly chosen 30s AUCs,

spread over the whole averaged recording, were generated and the actual EI was tested against the random sums. P-values lower than 0.05 were considered significant (Fig-6A and 6B). A P value <0.0015 indicated that the experimental EI was fully outside the range of all random EIs. A 10-second lag was incorporated for reverse command interneuron AVA. No lag was incorporated for sensory and first-layer interneurons (ASH, AWC, AIB). Neuronal activity correlations were calculated using Spearman's rank correlation test and corrected with Fisher's z-transformation before testing statistical significance (Mahadevan et al., 2021, Liégeois et al., 2020, Myers and Sirois, 2004), using custom R scripts.

Figure Legends

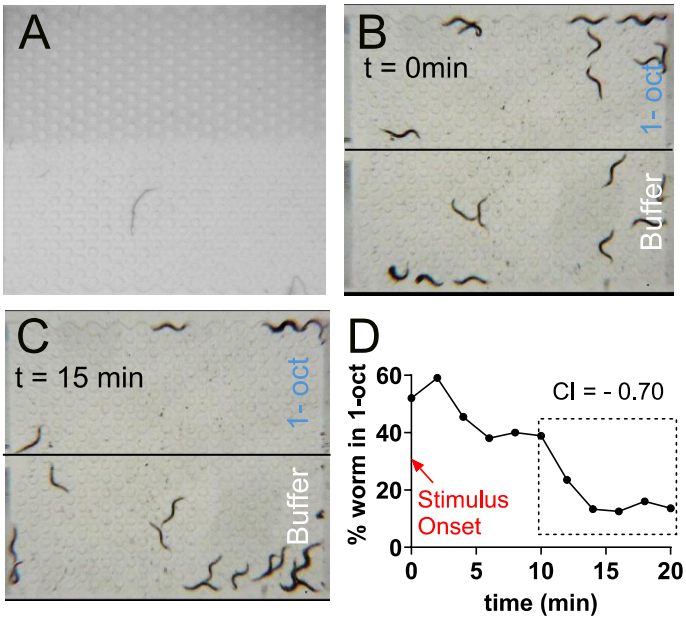

E

chemotaxis index (CI) =

$$\overline{X}_{t=10\text{-}20}\left(\frac{\#\text{ worms in stimulus} - \#\text{ worms in control buffer}}{\text{total }\#\text{ worms}}\right)$$

Figure 1. 1-oct chemotaxis in microfluidic arenas. A) Microfluidics arenas were configured with two zones of equal area, one containing a 1-oct solution and the other containing buffer alone (1-oct zone contains 0.01% xylene cyanol dye for visualization; assays are run without dye). B, C) typical distribution of worms when first exposed to 1-oct (B), and after 15 min of 1-oct exposure (C). D) Time-course of 1-oct chemotaxis. E) calculation of chemotaxis index, averaging worm counts every 2 minutes from 10-20 minutes after introduction of 1-oct solution.

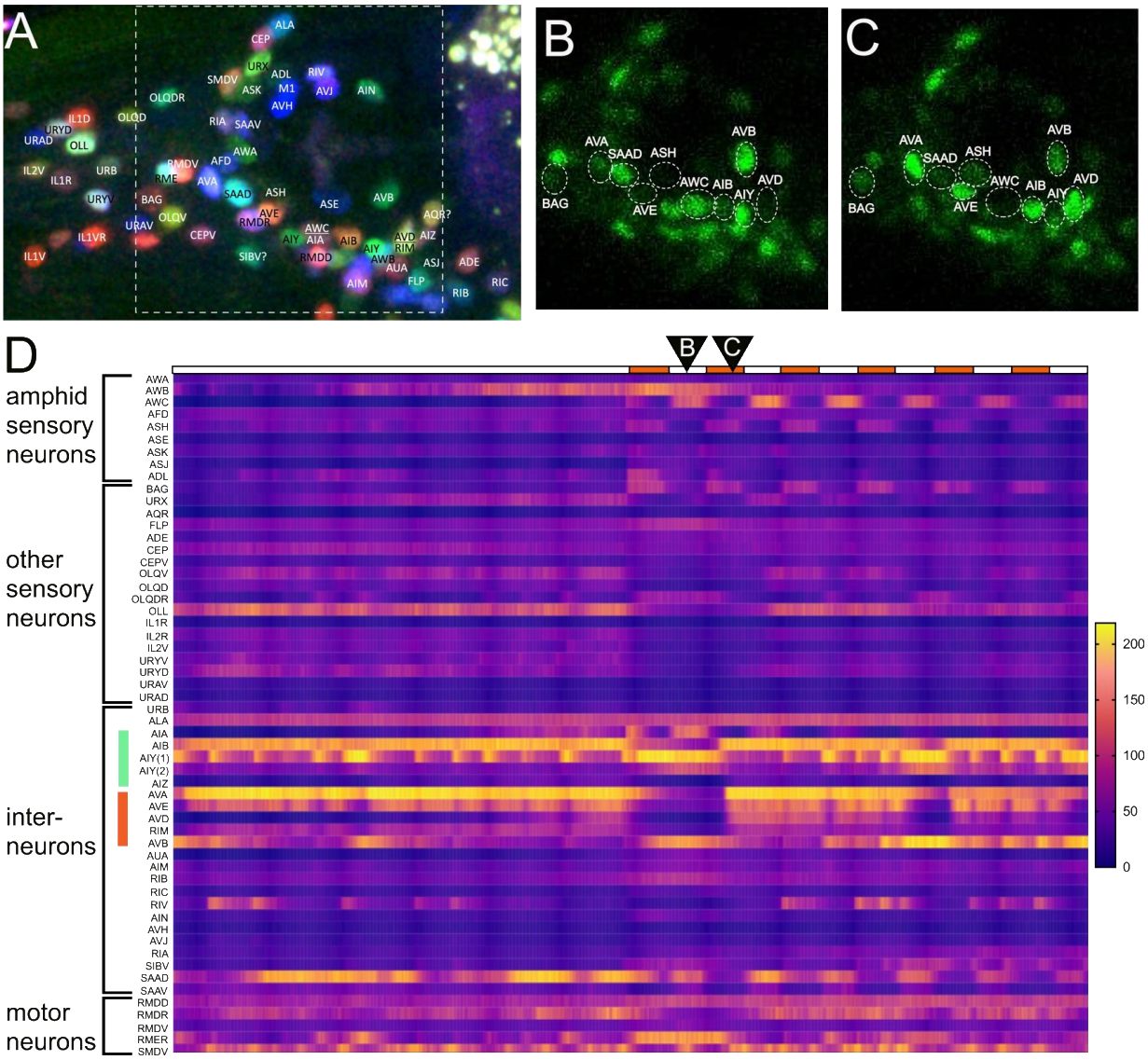

Figure 2. Network recording of 1-oct (2.2 mM) response. A) Representative image of a NeuroPAL worm immobilized in a microfluidics device visualized using the mTagBFP2, CyOFP, and mNeptune2.5 reporters for neuronal identification (Yemini et al., 2021). B, C) Pan-neuronal nGCaMP6s signal for the region indicated by the box in (A) during 1-oct stimulation, showing 1-oct offset (B) and onset (C). Specific time points in the recording for (B) and (C) are indicated by the black triangles in (D). Selected sensory neurons and interneurons are indicated by dashed white circles. D) Heat map of activity profiles for 56 identifiable neurons. Raw (i.e. non-normalized) fluorescence values shown. Stimulation time-course shown on top row (white is buffer, orange is 1-oct). Green and orange vertical bars at left indicate first-layer and locomotory command neurons (+RIM), respectively.

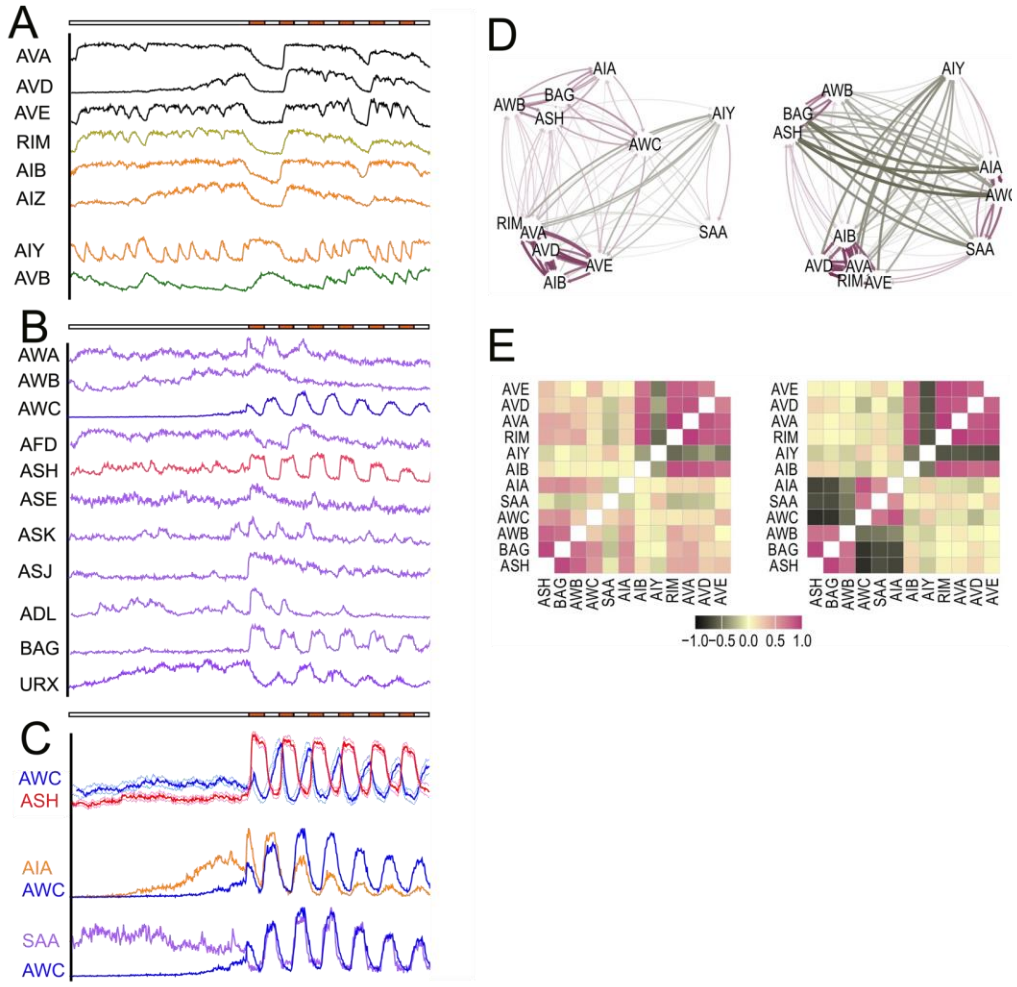

Figure 3. Neuronal activity correlations. A-C) Neuronal activity patterns from worm shown in Figure 2. A) Stochastic activity state transitions of locomotory command and associated interneurons, with AIY and AVB showing opposite activity patterns to AVA, AVD, AVE, RIM, AIB, and AIZ. B) Sensory neuron activity patterns. C) Selected neuron pairs highlighting the opposite activity patterns of AWC and ASH (top), and the correlated activity patterns of AWC with AIA (middle) and SAA (bottom). D, E) Activity correlations for 12 selected neurons based on data from 5 worms. D) Graph representation of activity correlations before stimulus (minutes 0-6, left) and during stimulus (minutes 6-12, right). Neurons pairs with the strongest positive correlations are closest to one another and connected by the darkest purple lines; neurons with the strongest negative correlations are furthest apart and connected by the darkest green lines. E) Relationships from (D) presented as a correlation matrix using the same color code.

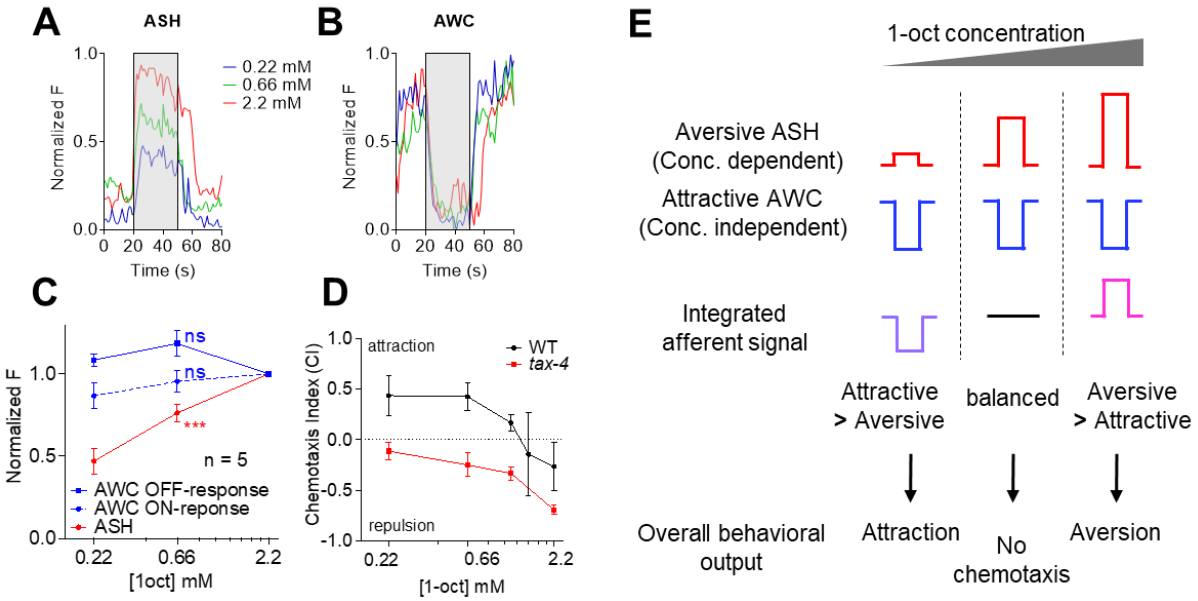

Figure 4. 1-oct valence reverses as a function of concentration. A-C) ASH ON responses (A, C) are concentration dependent, while AWC ON and OFF responses (B, C) are not, over a 10-fold concentration range from 0.22 to 2.2 mM. Representative traces from a single ASH or AWC neuron are shown (A, B, respectively), averages shown in (C) *** P<0.001, ns non-significant, paired ANOVA (Tukey's multiple comparison test). D) For wild type (black points/line), chemotaxis index for 1-oct switches from negative (repulsive) at the highest concentration (2.2 mM) to positive (attractive) at the lowest concentrations (0.22 and 0.66 mM), and insensitivity at intermediate concentrations (1.21 and 1.54 mM). In *tax-4* mutants, 1-oct responses are repulsive at all tested concentrations (red points/line), n = 3 -5. E) Results are consistent with a model in which repulsive and attractive afferent pathways (driven by ASH and AWC, respectively) are co-active, and balance to determine overall chemotactic response.

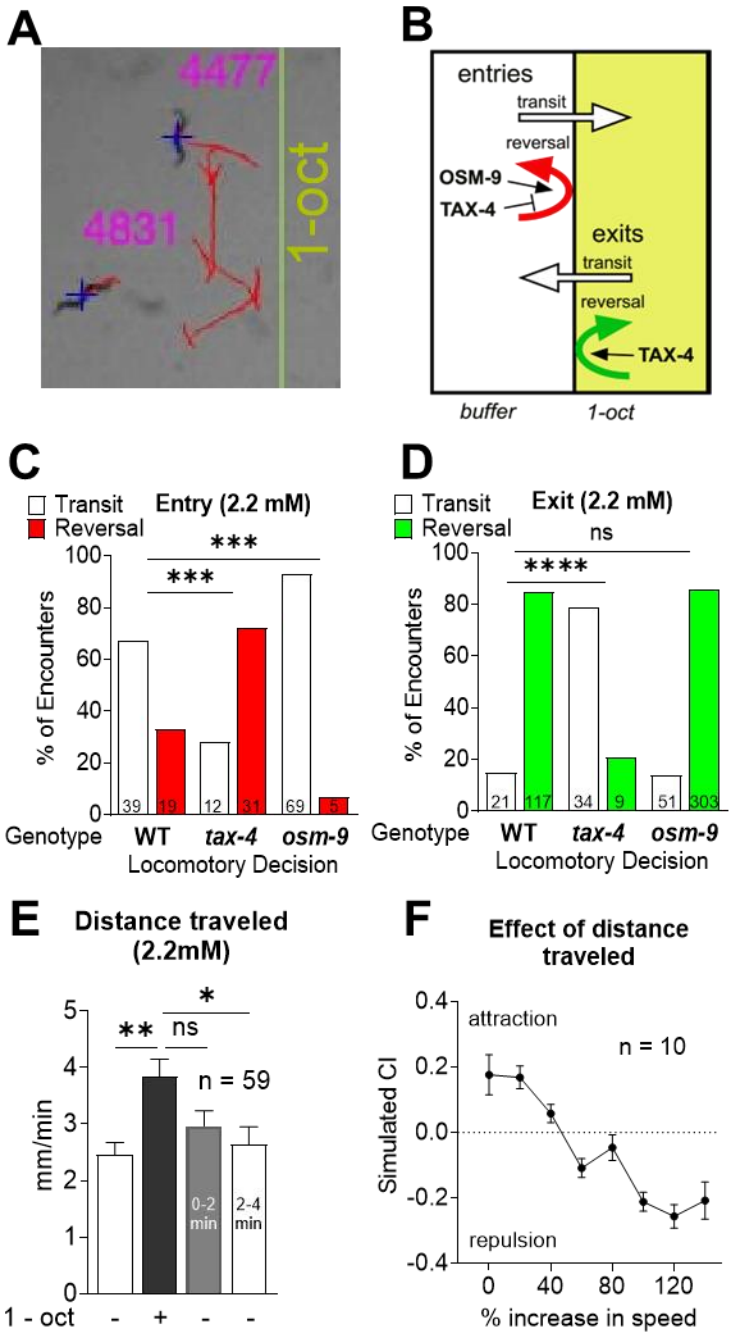

Figure 5. Locomotory reversals and speed modulation stimulated by 1-oct A) Example of a single worm track traced by the automated tracking software. B) Worms execute reversals probabilistically at the 1-oct-buffer interface dependent on TAX-4 and OSM-9 signaling cascades. C, D) Reversal probabilities at 1-oct-buffer interface for wild-type, *tax-4*, and *osm-9* (see panel B for summary and explanation of terms). C) movement from buffer zone to 1-oct zone ('entries'); D) movement from 1-oct zone to buffer zone ('exits'). E) Modulation of locomotory activity. Distance traveled in 2 minutes prior to, during, and after 1-oct exposure. F) Simulation of chemotaxis outcome based on reversal probabilities (from C, D) and locomotory activity modulation (from E). Points shown are averages of 10 simulation trials with SEM error bars. ***, **** in C, D indicate P<0.001, 0.0001 Fisher's Exact Test. *, ** in E indicate P<0.05, 0.01, ANOVA (Tukey's multiple comparison test).

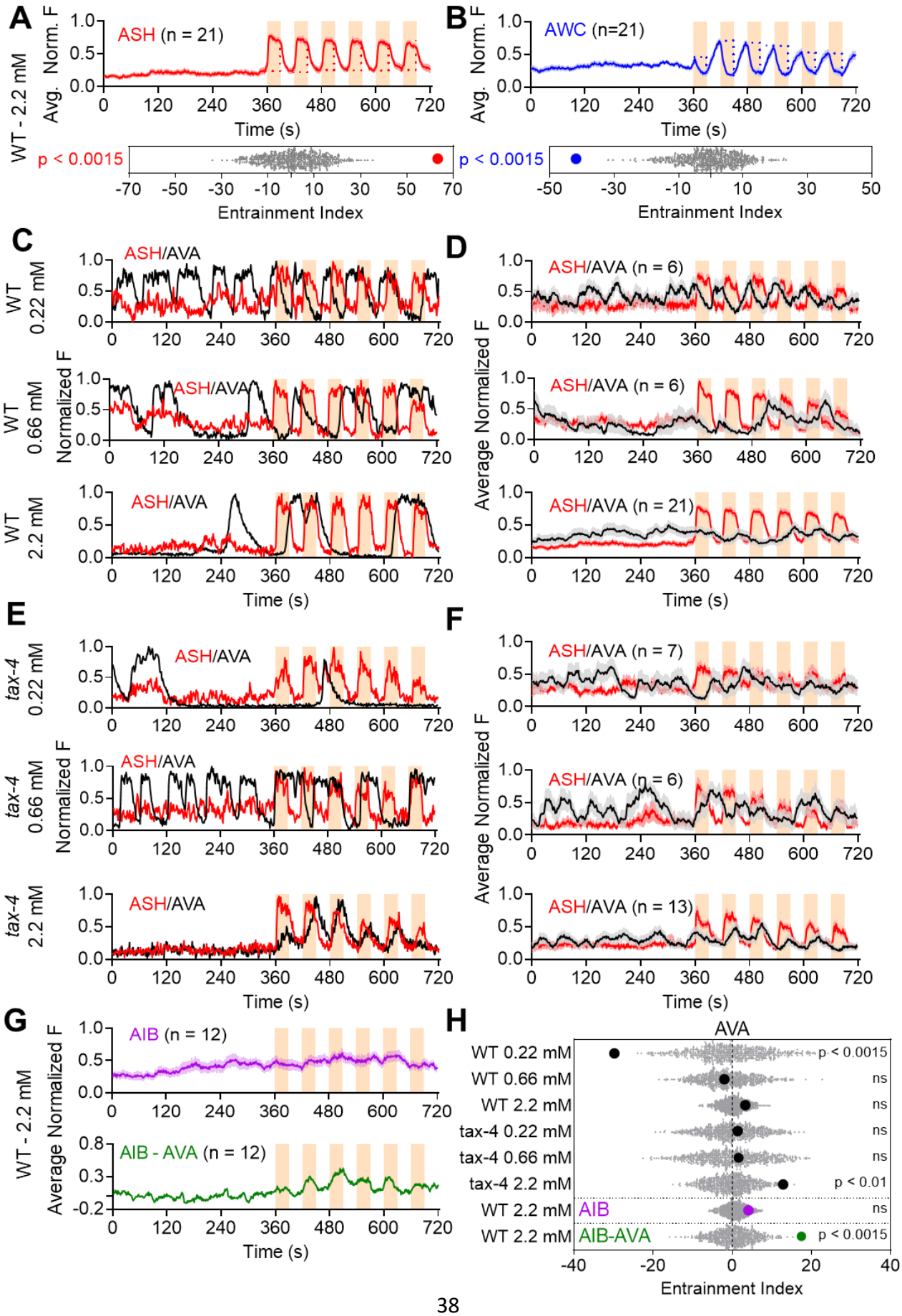
A
WT - 2.2 mM
Avg. Norm. F
ASH (n = 21)
Time (s)
p < 0.0015
Entrainment Index
B
Avg. Norm. F
AWC (n=21)
Time (s)
p < 0.0015
Entrainment Index
C
WT 0.22 mM
ASH/AVA
WT 0.66 mM
Normalized F
ASH/AVA
WT 2.2 mM
ASH/AVA
Time (s)
D
ASH/AVA (n = 6)
Average Normalized F
ASH/AVA (n = 6)
ASH/AVA (n = 21)
Time (s)
E
tax-4 0.22 mM
ASH/AVA
tax-4 0.66 mM
Normalized F
ASH/AVA
tax-4 2.2 mM
ASH/AVA
Time (s)
F
ASH/AVA (n = 7)
Average Normalized F
ASH/AVA (n = 6)
ASH/AVA (n = 13)
Time (s)
G
WT - 2.2 mM
Average Normalized F
AIB (n = 12)
AIB - AVA (n = 12)
Time (s)
H
AVA
WT 0.22 mM
WT 0.66 mM
WT 2.2 mM
tax-4 0.22 mM
tax-4 0.66 mM
tax-4 2.2 mM
WT 2.2 mM AIB
WT 2.2 mM AIB-AVA
p < 0.0015
ns
ns
ns
ns
p < 0.01
ns
p < 0.0015
Entrainment Index

Figure 6. Entrainment of neuronal activity by 1-oct stimulation. A, B) Validation of the entrainment index measurement using ASH (A) and AWC (B), showing very strong positive and very strong negative entrainment by 1-oct application, as expected. Gray dots indicate each randomized sum, while red and blue dots indicate the stimulus-specific sums of ASH and AWC, respectively (see Methods). C-F) Superimposed ASH and AVA activity patterns after stimulation by 0.22, 0.66, and 2.2 mM 1-oct in wild type (C, D) and *tax-4* (E, F). Single worm traces (C, E) and averaged traces are shown (D, F, n ranges from 6-21 worms). G) AIB trace (averaged); showing unprocessed (upper panel, purple trace) and AIB after subtracting AVA activity (lower panel, green trace). H) Entrainment indices for all recordings in C through G, with gray dots indicating randomized EIs and the bold dots represent the stimulus-specific EIs for AVA (black), unprocessed AIB (purple), and AVA-subtracted AIB (green). P values in A, B and H represent the probability that a randomized EI would be as great or greater than the stimulus-selected sum, with a significance cut-off of $P<0.05$.

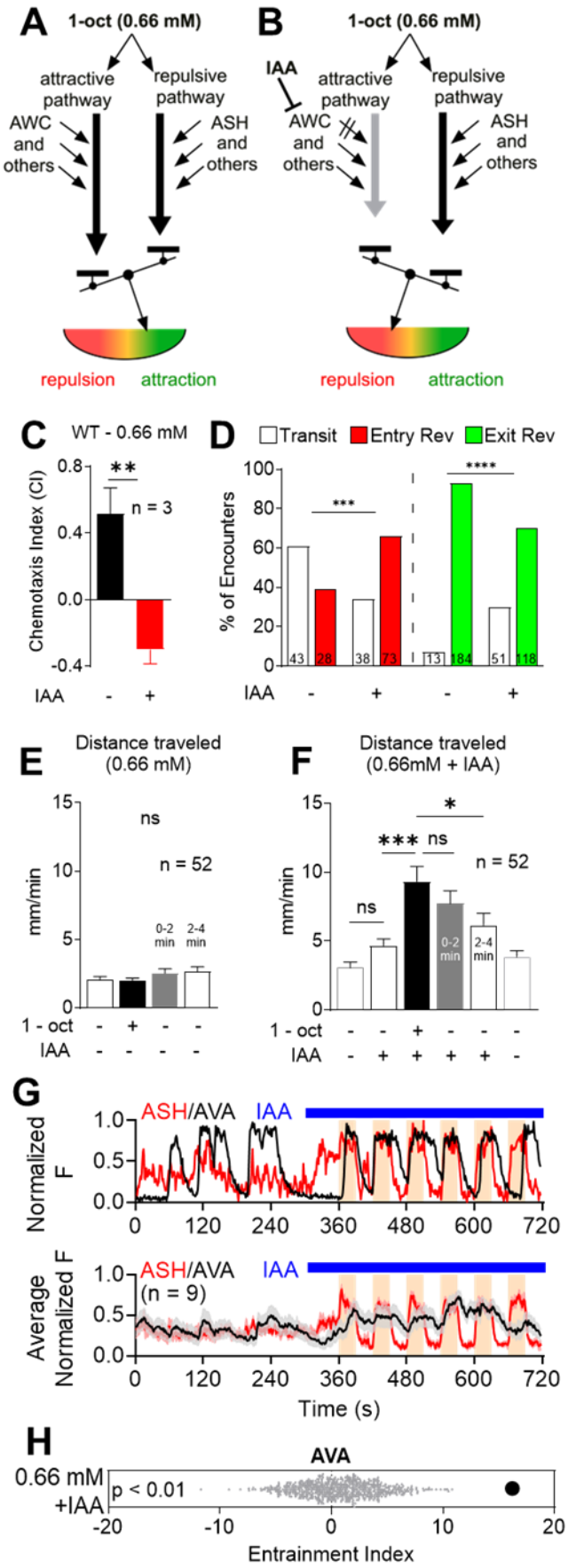

Figure 7. Balanced repulsion and attraction support context-dependent modulation of sensory responses. (A, B) Combinatorial coding-based mechanism for modulating sensory responses A) At lower 1-oct concentrations, the attractive afferent pathway is relatively strong, resulting in attraction. B) Addition of IAA reduces AWC activity, weakening the attractive pathway relative to the repulsive pathway, and reversing the 1-oct valence. C) Addition of 0.92 mM IAA reverses the valence of 1-oct (0.66 mM) from attractive to repulsive. D) IAA biases reversal behavior (at the 1-oct/buffer interface) toward repulsion. Reversals upon entering 1-oct zone are increased (left side/red), and reversals upon exiting the 1-oct zone are decreased (right side /green). (E-F) Effect of IAA on locomotory activity. E) 1-oct (0.66 mM) in the absence of IAA does not cause increased speed. F) 1-oct (0.66 mM) in the presence of IAA causes markedly increased speed. G) Single (upper) and averaged (lower) recordings of ASH and AVA before and after addition of IAA and 1-oct (0.66mM) as shown, demonstrating increased AVA entrainment to stimulus (compare to Fig-6D/middle). Blue bar indicates addition of IAA (in both control buffer and 1-oct solutions). H) AVA entrainment index confirms that the presence of IAA causes AVA to become significantly entrained with the stimulus. ** in C indicates P<0.01, *t-test*; *** and **** in D indicate P<0.001, 0.0001 respectively, Fisher's Exact Test; *, *** in F indicate P<0.05 and 0.001, respectively, ANOVA and Tukey's multiple comparison test.

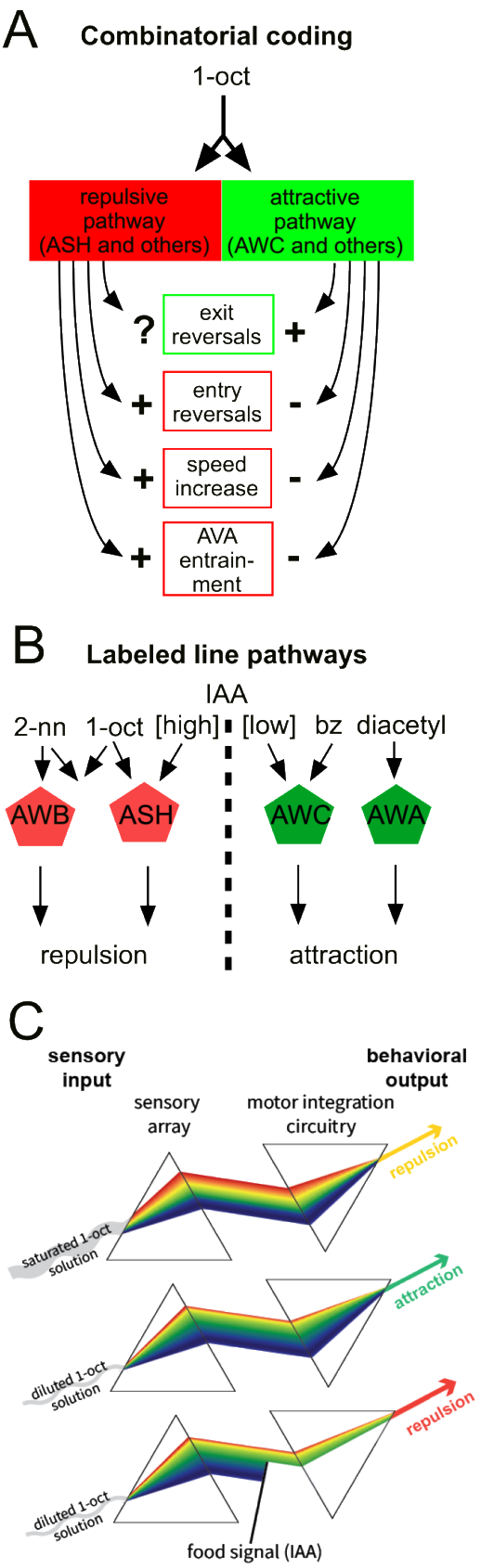

Figure 8. Olfactory combinatorial coding strategies for sensory motor coupling and context-dependent modulation in *C. elegans*. A) Summary of the combinatorial coding model. 1-oct simultaneously activates sensory neurons that mediate both repulsion (ASH and other) and attraction (AWC and others), such that repulsive and attractive afferent pathways become active concurrently. The outputs of these pathways are then integrated deeper in the sensory motor circuitry to control at least three key locomotory parameters (exit reversals, entry reversals, and locomotory speed), and the activity state of the reverse command neurons. This combinatorial scheme differs from the labeled line view of olfactory coding in *C. elegans* (B), in which odorants are considered either repellents or attractants, and the downstream behavioral outcome is determined at or near the sensory level, based on whether they activate attractive sensory neurons or repulsive sensory neurons. C) An analogy based on refraction on light through two prisms highlights the potential versatility of olfactory combinatorial coding in *C. elegans*. An individual odorant activates many chemosensory neurons to produce multiple distinct afferent inputs propagating through the downstream circuitry simultaneously, analogous to the first prism separating white light into its component colors (top panel, left). The motor integration circuity formulates a locomotory response by integrating the active afferent pathways, analogous to the second prism recombining the incoming light (top panel, right). Because chemosensory neurons have different odorant affinities, the specific outputs of the sensory array and motor integration circuit may be concentration dependent. In this study, ASH (coded in red) is a low affinity sensor, while AWC (coded in blue) is a high affinity sensor. Reducing the 1-oct concentration biases the output of the sensory array toward AWC (middle panel, left), and the motor integration circuitry uses this information to produce an attractive locomotory response

(middle panel, right). This coding strategy produces a simple framework for modulation. The behavioral outcome may be influenced by simply shifting the balance of the afferent pathways, much like an optical filter placed in a light path can selectively eliminate specific wavelengths (lower panel) to change the color of the transmitted light. In this study, IAA was added to the diluted 1-oct solution, inhibiting AWC, such that the afferent pathways were re-balanced toward the ASH end of the spectrum, and repulsion was restored. This 'filtering' effect could, in principle, take place at the sensory level or lower in the circuitry, and could subserve modulation due to the presence of other odorant molecules, or monoamine/neuropeptide modulators serving as interoceptive signals or effectors of experience-dependent plasticity.

References:

Albrecht, D. R. & Bargmann, C. I. 2011. High-content behavioral analysis of Caenorhabditis elegans in precise spatiotemporal chemical environments. *Nat Methods,* 8**,** 599-605.

Bargmann, C. I., Hartwieg, E. & Horvitz, H. R. 1993. Odorant-selective genes and neurons mediate olfaction in C. elegans. *Cell,* 74**,** 515-527.

Barretto, R. P., Gillis-Smith, S., Chandrashekar, J., Yarmolinsky, D. A., Schnitzer, M. J., Ryba, N. J. & Zuker, C. S. 2015. The neural representation of taste quality at the periphery. *Nature,* 517**,** 373-6.

Blazing, R. M. & Franks, K. M. 2020. Odor coding in piriform cortex: mechanistic insights into distributed coding. *Curr Opin Neurobiol,* 64**,** 96-102.

Bourgou, S., Rahali, F. Z., Ourghemmi, I. & Saïdani Tounsi, M. 2012. Changes of peel essential oil composition of four Tunisian citrus during fruit maturation. *ScientificWorldJournal,* 2012**,** 528593.

Brenner, S. 1974. The genetics of Caenorhabditis elegans. *Genetics,* 77**,** 71-94.

Bryant, H. L. & Segundo, J. P. 1976. Spike initiation by transmembrane current: a white-noise analysis. *The Journal of physiology,* 260**,** 279-314.

Buck, L. & Axel, R. 1991. A novel multigene family may encode odorant receptors: a molecular basis for odor recognition. *Cell,* 65**,** 175-187.

Bushdid, C., Magnasco, M. O., Vosshall, L. B. & Keller, A. 2014. Humans can discriminate more than 1 trillion olfactory stimuli. *Science,* 343**,** 1370-2.

Chalasani, S. H., Chronis, N., Tsunozaki, M., Gray, J. M., Ramot, D., Goodman, M. B. & Bargmann, C. I. 2007. Dissecting a circuit for olfactory behaviour in Caenorhabditis elegans. *Nature,* 450**,** 63-70.

Chalasani, S. H., Kato, S., Albrecht, D. R., Nakagawa, T., Abbott, L. & Bargmann, C. I. 2010. Neuropeptide feedback modifies odor-evoked dynamics in Caenorhabditis elegans olfactory neurons. *Nature neuroscience,* 13**,** 615-621.

Chalfie, M., Sulston, J. E., White, J. G., Southgate, E., Thomson, J. N. & Brenner, S. 1985. The neural circuit for touch sensitivity in Caenorhabditis elegans. *Journal of Neuroscience,* 5**,** 956-964.

Chao, M. Y., Komatsu, H., Fukuto, H. S., Dionne, H. M. & Hart, A. C. 2004. Feeding status and serotonin rapidly and reversibly modulate a Caenorhabditis elegans chemosensory circuit. *Proc Natl Acad Sci U S A,* 101**,** 15512-7.

Chronis, N., Zimmer, M. & Bargmann, C. I. 2007. Microfluidics for in vivo imaging of neuronal and behavioral activity in Caenorhabditis elegans. *Nat Methods,* 4**,** 727-31.

Coburn, C. M. & Bargmann, C. I. 1996. A putative cyclic nucleotide–gated channel is required for sensory development and function in C. elegans. *Neuron,* 17**,** 695-706.

Colbert, H. A., Smith, T. L. & Bargmann, C. I. 1997. OSM-9, A novel protein with structural similarity to channels, is required for olfaction, mechanosensation, and olfactory adaptation incaenorhabditis elegans. *Journal of Neuroscience,* 17**,** 8259-8269.

Dag, U., Nwabudike, I., Kang, D., Gomes, M. A., Kim, J., Atanas, A. A., Bueno, E., Estrem, C., Pugliese, S. & Wang, Z. 2023. Dissecting the functional organization of the C. elegans serotonergic system at whole-brain scale. *Cell,* 186**,** 2574-2592. e20.

Davidson, A. G., O'dell, R., Chan, V. & Schieber, M. H. 2007. Comparing effects in spike-triggered averages of rectified EMG across different behaviors. *J Neurosci Methods,* 163**,** 283-94.

De Boer, E. & Kuyper, P. 1968. Triggered correlation. *IEEE Transactions on Biomedical Engineering***,** 169-179.

Debnath, A., Williams, P. D. & Bamber, B. A. 2022. Reduced Ca2+ transient amplitudes may signify increased or decreased depolarization depending on the neuromodulatory signaling pathway. *Frontiers in Neuroscience,* 16**,** 931328.

Dikeçligil, G. N. & Gottfried, J. A. 2024. What Does the Human Olfactory System Do, and How Does It Do It? *Annual Review of Psychology,* 75**,** 155-181.

Dubbs, A., Guevara, J. & Yuste, R. 2016. moco: Fast Motion Correction for Calcium Imaging. *Front Neuroinform,* 10**,** 6.

Endo, K. & Kazama, H. 2022. Central organization of a high-dimensional odor space. *Curr Opin Neurobiol,* 73**,** 102528.

Ezak, M. J., Hong, E., Chaparro-Garcia, A. & Ferkey, D. M. 2010. Caenorhabditis elegans TRPV channels function in a modality-specific pathway to regulate response to aberrant sensory signaling. *Genetics,* 185**,** 233-244.

Ferkey, D. M., Sengupta, P. & L'etoile, N. D. 2021. Chemosensory signal transduction in Caenorhabditis elegans. *Genetics,* 217.

Fryer, E., Guha, S., Rogel-Hernandez, L. E., Logan-Garbisch, T., Farah, H., Rezaei, E., Mollhoff, I. N., Nekimken, A. L., Xu, A., Selin Seyahi, L., Fechner, S., Druckmann, S., Clandinin, T. R., Rhee, S. Y. & Goodman, M. B. 2024. An efficient behavioral screening platform classifies natural products and other chemical cues according to their chemosensory valence in C. elegans. *bioRxiv*.

Ghosh, D. D., Sanders, T., Hong, S., Mccurdy, L. Y., Chase, D. L., Cohen, N., Koelle, M. R. & Nitabach, M. N. 2016. Neural architecture of hunger-dependent multisensory decision making in C. elegans. *Neuron,* 92**,** 1049-1062.

Gordus, A., Pokala, N., Levy, S., Flavell, S. W. & Bargmann, C. I. 2015. Feedback from network states generates variability in a probabilistic olfactory circuit. *Cell,* 161**,** 215-27.

Gray, J. M., Hill, J. J. & Bargmann, C. I. 2005. A circuit for navigation in Caenorhabditis elegans. *Proc Natl Acad Sci U S A,* 102**,** 3184-91.

Greene, J. S., Dobosiewicz, M., Butcher, R. A., Mcgrath, P. T. & Bargmann, C. I. 2016. Regulatory changes in two chemoreceptor genes contribute to a Caenorhabditis elegans QTL for foraging behavior. *elife,* 5**,** e21454.

Grothe, B., Pecka, M. & Mcalpine, D. 2010. Mechanisms of sound localization in mammals. *Physiological reviews,* 90**,** 983-1012.

Ha, H.-I., Hendricks, M., Shen, Y., Gabel, C. V., Fang-Yen, C., Qin, Y., Colon-Ramos, D., Shen, K., Samuel, A. D. & Zhang, Y. 2010. Functional organization of a neural network for aversive olfactory learning in Caenorhabditis elegans. *Neuron,* 68**,** 1173-1186.

Hallinen, K. M., Dempsey, R., Scholz, M., Yu, X., Linder, A., Randi, F., Sharma, A. K., Shaevitz, J. W. & Leifer, A. M. 2021. Decoding locomotion from population neural activity in moving C. elegans. *Elife,* 10**,** e66135.

Hammarlund, M., Hobert, O., Miller, D. M. & Sestan, N. 2018. The CeNGEN project: the complete gene expression map of an entire nervous system. *Neuron,* 99**,** 430-433.

Hapiak, V., Summers, P., Ortega, A., Law, W. J., Stein, A. & Komuniecki, R. 2013. Neuropeptides amplify and focus the monoaminergic inhibition of nociception in Caenorhabditis elegans. *Journal of Neuroscience,* 33**,** 14107-14116.

Horio, N., Murata, K., Yoshikawa, K., Yoshihara, Y. & Touhara, K. 2019. Contribution of individual olfactory receptors to odor-induced attractive or aversive behavior in mice. *Nature communications,* 10**,** 209.

Hukema, R. K., Rademakers, S., Dekkers, M. P., Burghoorn, J. & Jansen, G. 2006. Antagonistic sensory cues generate gustatory plasticity in Caenorhabditis elegans. *EMBO J,* 25**,** 312-22.

Im Choi, J., Lee, H. K., Kim, H. S., Park, S. Y., Lee, T. Y., Yoon, K.-H. & Lee, J. I. 2018. Odor-dependent temporal dynamics in Caenorhabitis elegans adaptation and aversive learning behavior. *PeerJ,* 6**,** e4956.

Itskovits, E., Levine, A., Cohen, E. & Zaslaver, A. 2017. A multi-animal tracker for studying complex behaviors. *BMC biology,* 15**,** 1-16.

Itskovits, E., Ruach, R., Kazakov, A. & Zaslaver, A. 2018. Concerted pulsatile and graded neural dynamics enables efficient chemotaxis in C. elegans. *Nat Commun,* 9**,** 2866.

Jang, H., Kim, K., Neal, S. J., Macosko, E., Kim, D., Butcher, R. A., Zeiger, D. M., Bargmann, C. I. & Sengupta, P. 2012. Neuromodulatory state and sex specify alternative behaviors through antagonistic synaptic pathways in C. elegans. *Neuron,* 75**,** 585-592.

Ji, N., Venkatachalam, V., Rodgers, H. D., Hung, W., Kawano, T., Clark, C. M., Lim, M., Alkema, M. J., Zhen, M. & Samuel, A. D. 2021. Corollary discharge promotes a sustained motor state in a neural circuit for navigation. *Elife,* 10**,** e68848.

Kato, S., Kaplan, H. S., Schrödel, T., Skora, S., Lindsay, T. H., Yemini, E., Lockery, S. & Zimmer, M. 2015. Global brain dynamics embed the motor command sequence of Caenorhabditis elegans. *Cell,* 163**,** 656-69.

Katz, M., Corson, F., Keil, W., Singhal, A., Bae, A., Lu, Y., Liang, Y. & Shaham, S. 2019. Glutamate spillover in C. elegans triggers repetitive behavior through presynaptic activation of MGL-2/mGluR5. *Nature Communications,* 10**,** 1882.

Khan, M., Hartmann, A. H., O'donnell, M. P., Piccione, M., Pandey, A., Chao, P.-H., Dwyer, N. D., Bargmann, C. I. & Sengupta, P. 2022. Context-dependent reversal of odorant preference is driven by inversion of the response in a single sensory neuron type. *PLoS biology,* 20**,** e3001677.

Kotera, I., Tran, N. A., Fu, D., Kim, J. H., Byrne Rodgers, J. & Ryu, W. S. 2016. Pan-neuronal screening in Caenorhabditis elegans reveals asymmetric dynamics of AWC neurons is critical for thermal avoidance behavior. *elife,* 5**,** e19021.

Kuramochi, M. & Doi, M. 2017. A Computational Model Based on Multi-Regional Calcium Imaging Represents the Spatio-Temporal Dynamics in a Caenorhabditis elegans Sensory Neuron. *PLoS One,* 12**,** e0168415.

Lagoy, R. C. & Albrecht, D. R. 2015. Microfluidic devices for behavioral analysis, microscopy, and neuronal imaging in Caenorhabditis elegans. *C. elegans: Methods and Applications***,** 159-179.

Li, Z., Zhou, J., Wani, K. A., Yu, T., Ronan, E. A., Piggott, B. J., Liu, J. & Xu, X. S. 2023. A C. elegans neuron both promotes and suppresses motor behavior to fine tune motor output. *Frontiers in Molecular Neuroscience,* 16.

Liégeois, R., Santos, A., Matta, V., Van De Ville, D. & Sayed, A. H. 2020. Revisiting correlation-based functional connectivity and its relationship with structural connectivity. *Network Neuroscience,* 4**,** 1235-1251.

Lin, A., Qin, S., Casademunt, H., Wu, M., Hung, W., Cain, G., Tan, N. Z., Valenzuela, R., Lesanpezeshki, L., Venkatachalam, V., Pehlevan, C., Zhen, M. & Samuel, A. D. T. 2023. Functional imaging and quantification of multineuronal olfactory responses in C. elegans. *Sci Adv,* 9**,** eade1249.

Lockery, S. R., Lawton, K. J., Doll, J. C., Faumont, S., Coulthard, S. M., Thiele, T. R., Chronis, N., Mccormick, K. E., Goodman, M. B. & Pruitt, B. L. 2008. Artificial dirt: microfluidic substrates for nematode neurobiology and behavior. *Journal of neurophysiology,* 99**,** 3136-3143.

Mahadevan, A. S., Tooley, U. A., Bertolero, M. A., Mackey, A. P. & Bassett, D. S. 2021. Evaluating the sensitivity of functional connectivity measures to motion artifact in resting-state fMRI data. *NeuroImage,* 241**,** 118408.

Malnic, B., Hirono, J., Sato, T. & Buck, L. B. 1999. Combinatorial receptor codes for odors. *Cell,* 96**,** 713-723.

Meng, J., Ahamed, T., Yu, B., Hung, W., Ei Mouridi, S., Wang, Z., Zhang, Y., Wen, Q., Boulin, T. & Gao, S. 2024. A tonically active master neuron modulates mutually exclusive motor states at two timescales. *Science Advances,* 10**,** eadk0002.

Mombaerts, P., Wang, F., Dulac, C., Chao, S. K., Nemes, A., Mendelsohn, M., Edmondson, J. & Axel, R. 1996. Visualizing an olfactory sensory map. *Cell,* 87**,** 675-86.

Mori, K. & Sakano, H. 2021. Olfactory Circuitry and Behavioral Decisions. *Annu Rev Physiol,* 83**,** 231-256.

Mueller, K. L., Hoon, M. A., Erlenbach, I., Chandrashekar, J., Zuker, C. S. & Ryba, N. J. 2005. The receptors and coding logic for bitter taste. *Nature,* 434**,** 225-229.

Murayama, T. & Maruyama, I. N. 2013. Decision making in C. elegans chemotaxis to alkaline pH: Competition between two sensory neurons, ASEL and ASH. *communicative & integrative Biology,* 6**,** 1007-12.

Myers, L. & Sirois, M. J. 2004. Spearman correlation coefficients, differences between. *Encyclopedia of statistical sciences,* 12.

Neelakandan, P., Young, C.-C., Hameed, A., Wang, Y.-N., Chen, K.-N. & Shen, F.-T. 2021. Volatile 1-octanol of tea (Camellia sinensis L.) fuels cell division and indole-3-acetic acid production in phylloplane isolate Pseudomonas sp. NEEL19. *Scientific Reports,* 11**,** 2788.

Nguyen, J. P., Shipley, F. B., Linder, A. N., Plummer, G. S., Liu, M., Setru, S. U., Shaevitz, J. W. & Leifer, A. M. 2016. Whole-brain calcium imaging with cellular resolution in freely behaving Caenorhabditis elegans. *Proceedings of the National Academy of Sciences,* 113**,** E1074-E1081.

Nichols, A. L., Eichler, T., Latham, R. & Zimmer, M. 2017. A global brain state underlies C. elegans sleep behavior. *Science,* 356**,** eaam6851.

Ouellette, M.-H., Desrochers, M. J., Gheta, I., Ramos, R. & Hendricks, M. 2018. A gate-and-switch model for head orientation behaviors in Caenorhabditis elegans. *Eneuro,* 5.

Piggott, B. J., Liu, J., Feng, Z., Wescott, S. A. & Xu, X. S. 2011. The neural circuits and synaptic mechanisms underlying motor initiation in C. elegans. *Cell,* 147**,** 922-933.

Prevedel, R., Yoon, Y.-G., Hoffmann, M., Pak, N., Wetzstein, G., Kato, S., Schrödel, T., Raskar, R., Zimmer, M. & Boyden, E. S. 2014. Simultaneous whole-animal 3D imaging of neuronal activity using light-field microscopy. *Nature methods,* 11**,** 727-730.

Rengarajan, S. & Hallem, E. A. 2016. Olfactory circuits and behaviors of nematodes. *Current Opinion in Neurobiology,* 41**,** 136-148.

Riedl, J., Fieseler, C. & Zimmer, M. 2022. Tyraminergic corollary discharge filters reafferent perception in a chemosensory neuron. *Curr Biol,* 32**,** 3048-3058.e6.

Roper, S. D. & Chaudhari, N. 2017. Taste buds: cells, signals and synapses. *Nature Reviews Neuroscience,* 18**,** 485-497.

Saito, H., Nishizumi, H., Suzuki, S., Matsumoto, H., Ieki, N., Abe, T., Kiyonari, H., Morita, M., Yokota, H., Hirayama, N., Yamazaki, T., Kikusui, T., Mori, K. & Sakano, H. 2017. Immobility responses are induced by photoactivation of single glomerular species responsive to fox odour TMT. *Nat Commun,* 8**,** 16011.

Schindelin, J., Arganda-Carreras, I., Frise, E., Kaynig, V., Longair, M., Pietzsch, T., Preibisch, S., Rueden, C., Saalfeld, S., Schmid, B., Tinevez, J. Y., White, D. J., Hartenstein, V., Eliceiri, K., Tomancak, P. & Cardona, A. 2012. Fiji: an open-source platform for biological-image analysis. *Nat Methods,* 9**,** 676-82.

Schneider, C. A., Rasband, W. S. & Eliceiri, K. W. 2012. NIH Image to ImageJ: 25 years of image analysis. *Nat Methods,* 9**,** 671-5.

Schrödel, T., Prevedel, R., Aumayr, K., Zimmer, M. & Vaziri, A. 2013. Brain-wide 3D imaging of neuronal activity in Caenorhabditis elegans with sculpted light. *Nature methods,* 10**,** 1013-1020.

Sordillo, A. & Bargmann, C. I. 2021. Behavioral control by depolarized and hyperpolarized states of an integrating neuron. *Elife,* 10**,** e67723.

Stiernagle, T. 2006. Maintenance of C. elegans. WormBook. The C. elegans research community. *WormBook*.

Taylor, S. R., Santpere, G., Weinreb, A., Barrett, A., Reilly, M. B., Xu, C., Varol, E., Oikonomou, P., Glenwinkel, L. & Mcwhirter, R. 2021. Molecular topography of an entire nervous system. *Cell,* 184**,** 4329-4347. e23.

Toyoshima, Y., Wu, S., Kanamori, M., Sato, H., Jang, M. S., Oe, S., Murakami, Y., Teramoto, T., Park, C. & Iwasaki, Y. 2020. Neuron ID dataset facilitates neuronal annotation for whole-brain activity imaging of C. elegans. *BMC biology,* 18**,** 1-20.

Troemel, E. R., Chou, J. H., Dwyer, N. D., Colbert, H. A. & Bargmann, C. I. 1995. Divergent seven transmembrane receptors are candidate chemosensory receptors in C. elegans. *Cell,* 83**,** 207-18.

Troemel, E. R., Kimmel, B. E. & Bargmann, C. I. 1997. Reprogramming chemotaxis responses: sensory neurons define olfactory preferences in C. elegans. *Cell,* 91**,** 161-169.

Tsunozaki, M., Chalasani, S. H. & Bargmann, C. I. 2008. A behavioral switch: cGMP and PKC signaling in olfactory neurons reverses odor preference in C. elegans. *Neuron,* 59**,** 959-971.

Venkatachalam, V., Ji, N., Wang, X., Clark, C., Mitchell, J. K., Klein, M., Tabone, C. J., Florman, J., Ji, H. & Greenwood, J. 2016. Pan-neuronal imaging in roaming Caenorhabditis elegans. *Proceedings of the National Academy of Sciences,* 113**,** E1082-E1088.

Wang, Y., Zhang, X., Xin, Q., Hung, W., Florman, J., Huo, J., Xu, T., Xie, Y., Alkema, M. J., Zhen, M. & Wen, Q. 2020. Flexible motor sequence generation during stereotyped escape responses. *Elife,* 9.

White, J. 2018. Clues to basis of exploratory behaviour of the C. elegans snout from head somatotropy. *Philos Trans R Soc Lond B Biol Sci,* 373.

White, J. G., Southgate, E., Thomson, J. N. & Brenner, S. 1986. The structure of the nervous system of the nematode Caenorhabditis elegans. *Philos Trans R Soc Lond B Biol Sci,* 314**,** 1-340.

Williams, P. D., Zahratka, J. A., Rodenbeck, M., Wanamaker, J., Linzie, H. & Bamber, B. A. 2018. Serotonin disinhibits a Caenorhabditis elegans sensory neuron by suppressing Ca2+-dependent negative feedback. *Journal of Neuroscience,* 38**,** 2069-2080.

Wirak, G. S., Florman, J., Alkema, M. J., Connor, C. W. & Gabel, C. V. 2022. Age-associated changes to neuronal dynamics involve a disruption of excitatory/inhibitory balance in C. elegans. *Elife,* 11**,** e72135.

Witvliet, D., Mulcahy, B., Mitchell, J. K., Meirovitch, Y., Berger, D. R., Wu, Y., Liu, Y., Koh, W. X., Parvathala, R. & Holmyard, D. 2021. Connectomes across development reveal principles of brain maturation. *Nature,* 596**,** 257-261.

Wojtyniak, M., Brear, A. G., O'halloran, D. M. & Sengupta, P. 2013. Cell- and subunit-specific mechanisms of CNG channel ciliary trafficking and localization in C. elegans. *J Cell Sci,* 126**,** 4381-95.

Wragg, R. T., Hapiak, V., Miller, S. B., Harris, G. P., Gray, J., Komuniecki, P. R. & Komuniecki, R. W. 2007. Tyramine and octopamine independently inhibit serotonin-stimulated aversive behaviors in Caenorhabditis elegans through two novel amine receptors. *Journal of Neuroscience,* 27**,** 13402-13412.

Yarmolinsky, D. A., Zuker, C. S. & Ryba, N. J. 2009. Common sense about taste: from mammals to insects. *Cell,* 139**,** 234-44.

Yemini, E., Lin, A., Nejatbakhsh, A., Varol, E., Sun, R., Mena, G. E., Samuel, A. D. T., Paninski, L., Venkatachalam, V. & Hobert, O. 2021. NeuroPAL: A Multicolor Atlas for Whole-Brain Neuronal Identification in C. elegans. *Cell,* 184**,** 272-288.e11.

Yoshida, K., Hirotsu, T., Tagawa, T., Oda, S., Wakabayashi, T., Iino, Y. & Ishihara, T. 2012. Odour concentration-dependent olfactory preference change in C. elegans. *Nature communications,* 3**,** 739.

Yu, X., Creamer, M. S., Randi, F., Sharma, A. K., Linderman, S. W. & Leifer, A. M. 2021. Fast deep neural correspondence for tracking and identifying neurons in C. elegans using semi-synthetic training. *Elife,* 10.

Zahratka, J. A., Williams, P. D., Summers, P. J., Komuniecki, R. W. & Bamber, B. A. 2015. Serotonin differentially modulates Ca2+ transients and depolarization in a C. elegans nociceptor. *J Neurophysiol,* 113**,** 1041-50.